Asymmetry dependence of nucleon correlations in spherical nuclei extracted from a dispersive-optical-model analysis

J. M. Mueller,[1,*] R. J. Charity,[2] R. Shane,[1] L. G. Sobotka,[1,2] S. J. Waldecker,[1] W. H. Dickhoff,[1] A. S. Crowell,[3] J. H. Esterline,[3] B. Fallin,[3] C. R. Howell,[3] C. Westerfeldt,[3] M. Youngs,[4] B. J. Crowe III,[5] and R. S. Pedroni[6]

[1]*Department of Physics, Washington University, St. Louis, Missouri 63130, USA*
[2]*Department of Chemistry, Washington University, St. Louis, Missouri 63130, USA*
[3]*Department of Physics, Duke University and Triangle Universities Nuclear Laboratory, Durham, North Carolina 27708, USA*
[4]*National Superconducting Cyclotron Laboratory and Department of Physics and Astronomy, Michigan State University, East Lansing, Michigan 48824, USA*
[5]*North Carolina Central University, Durham, North Carolina 27707, USA*
[6]*North Carolina A&T State University and Triangle Universities Nuclear Laboratory, Greensboro, North Carolina 27411, USA*

Neutron elastic-scattering angular distributions were measured at beam energies of 11.9 and 16.9 MeV on ^{40,48}Ca targets. These data plus other elastic-scattering measurements, total and reaction cross-sections measurements, $(e, e'p)$ data, and single-particle energies for magic and doubly magic nuclei have been analyzed in the dispersive optical-model (DOM), generating nucleon self-energies (optical-model potentials) that can be related, via the many-body Dyson equation, to spectroscopic factors and occupation probabilities. It is found that, for stable nuclei with $N \geqslant Z$, the imaginary surface potential for protons exhibits a strong dependence on the neutron-proton asymmetry. This result leads to a more modest dependence of the spectroscopic factors on asymmetry. The measured data and the DOM analysis of all considered nuclei clearly demonstrate that the neutron imaginary surface potential displays very little dependence on the neutron-proton asymmetry for nuclei near stability ($N \geqslant Z$).

PACS number(s): 21.10.Pc, 24.10.Ht, 25.40.Dn, 27.40.+z

I. INTRODUCTION

Mean-field quantum-mechanical orbits account for a large fraction of the properties of valence nucleons. The spectroscopic factors, the overlap integral between the A and the $A - 1$ (or $A + 1$) wave functions for hole (particle) states, provide a quantitative measure of the strength residing in these independent-particle-model (IPM) orbits. For closed-shell stable nuclei, $(e, e'p)$ measurements at NIKHEF have demonstrated that $\simeq 65\%$ of the strength is found in the IPM orbits [1]. The remaining strength has been moved to higher and lower energies by the influence of both long- and short-range correlations.

Short-range correlations are dominated by p-n interactions [2–4] and produce high-momentum components below the Fermi energy [5] and push strength from IPM orbits out to very large energies (by many hundreds of MeV) [6]. The strong p-n interactions, a consequence of the tensor force, imply a dependence of these short-range correlations on the proton-neutron asymmetry. Protons will feel stronger correlations in a neutron-rich nucleus and vice versa. This asymmetry dependence is predicted to give rise to a modest asymmetry dependence of the occupation probabilities in infinite nuclear matter [7,8].

Long-range correlations, associated with the coupling to the collective motion of nucleons, spread strength out more modestly, i.e., out to roughly 50 MeV from the IPM

value. Experimentally, the asymmetry dependence for protons appears to be much stronger than expected on the basis of short-range correlations [9]. Although a theoretical understanding is lacking, it is clear that the enhancement over the short-range effects occurs in the domain where surface excitations dominate.

Experimental spectroscopic factors derived from the eikonal analysis of heavy-ion knockout reactions apparently exhibit a very strong asymmetry dependence [10,11]. The extreme example is for ^{32}Ar, where the $0d_{5/2}$ valence neutron hole level has a spectroscopic factor of about 21% of the IPM value. More recent measurements of transfer reactions generate spectroscopic factors that are in contradiction with these results [12] and indicate only a small or moderate dependence on nucleon asymmetry.

Current and future radioactive beam facilities will have to exclusively rely on hadronic reactions to extract such information since more weakly interacting probes such as the $(e, e'p)$ reaction can not be employed. In view of the present disagreement between the interpretation of the transfer and knockout measurements, it is important to identify methods that can uniquely determine correlation effects exhibited, for example, by spectroscopic factors as well as identify the origin of the implied correlations. This issue is already conspicuous because spectroscopic factors derived from different optical potentials in the analysis of transfer reactions generate differences as large as 30%, although the asymmetry dependence is similar [12].

Information about correlations is contained in the nucleon self-energy, which is a nonlocal and energy-dependent one-body potential that determines the nucleon single-particle

---

*Now at Department of Physics, Duke University, Durham, North Carolina 27708.

propagator from the Dyson equation [13]. The nucleon self-energy is complex and its real part can be obtained from its imaginary part by a dispersion relation and a correlated Hartree-Fock contribution that is energy independent. The Dyson equation generates both the properties of the system when a nucleon is added to the ground state or when one is removed. The nucleon self-energy, therefore, determines the elastic nucleon scattering cross section when it is iterated to all orders into the corresponding $\mathcal{T}$ matrix. The solution of the Dyson equation also generates the bound-state energies that can be reached by adding or removing a particle from the ground state, as well as the corresponding overlap functions that are normalized by the spectroscopic factors. Finally, the solution of the Dyson equation also generates the hole spectral function or removal probability (energy) density for energies in the continuum of the $A - 1$ system.

Traditionally, the term optical-model potential has been employed to describe a complex, energy-dependent, usually local, one-body potential that describes the elastic scattering of a nucleon for positive energies. In the dispersive optical model developed by Mahaux and Sartor [14], the optical-model (OM) potential is also considered for negative energies and causality is enforced by a dispersion relation, which links the real and imaginary potentials. With this model, the OM potential can be fit to both elastic-scattering data as well as bound-state properties. The fitted potential can be considered as a local approximation to the self-energy with a scaled imaginary potential. The latter scaling is also a consequence of the local approximation (Sec. III A). Ultimately, a real nonlocal potential is required before the full utility of the self-energy can be realized. It was shown recently [15] that replacing the energy-dependent local Hartree-Fock contribution to the real OM potential by a nonlocal potential (without energy dependence) allows for an interpretation of the DOM potential as a proper self-energy provided a well-defined reverse scaling is made to the imaginary part [14,15]. Because of their intimate connection, we will employ the two terms self-energy and optical potential interchangeably in the following.

An accurate determination of the nucleon self-energy both above and below the Fermi energy for a wide range of nuclei is essential for the reliable extraction of correlation effects as expressed in terms of spectroscopic factors when hadronic reactions are employed. We point again to the present uncertainty of at least 30% based on the choice of the optical potential used in the analysis of the (d, p) transfer reactions [12] as a case in point. We also note that, in the adiabatic wave approximation [16] employed for the analysis of this reaction, proton and neutron optical potentials are used at half the deuteron energy to describe the deuteron distorted wave, as well as overlap functions for the added or removed neutron. Since these quantities are part of the DOM framework, the future analysis of transfer reactions may profit from a unified approach and yield a more consistent description of spectroscopic factors.

Given the disagreement between the asymmetry dependences of spectroscopic factors deduced in knockout and transfer reactions, the DOM provides an alternative route to explore this physics. From experimental studies of the asymmetry dependence of the DOM potential one can, via the Dyson equation or the approximate expressions of Mahaux and Sartor, deduce the asymmetry dependence of the spectroscopic factors.

In a standard DOM analysis, one parametrizes the real and imaginary potentials based on theoretical expectations and past experimental work and constrains these parameters via fits to elastic-scattering measurements, reaction and total cross sections, and bound-state data. Our previous work on the Ca isotopes [17] showed that the imaginary surface potential for protons increased strongly with neutron excess. This implied a modest decrease in the spectroscopic factors of the valence levels with asymmetry, i.e., protons experience stronger correlations with increasing neutron number for neutron-rich systems. This trend is qualitatively consistent with those deduced from heavy-ion knockout reactions, but the magnitude is significantly smaller, which is much more in line with the results from transfer reactions and microscopic calculations using the Faddeev random-phase approximation [18].

The overall nucleon asymmetry dependence of the magnitude of the imaginary surface potential has been parametrized in global optical-model fits [19–21] according to

$$W^{\text{sur}} = W_0^{\text{sur}} \pm W_1^{\text{sur}} \frac{N - Z}{A}, \qquad (1)$$

where the plus sign refers to protons and the minus to neutrons. This form is based on the Lane potential [22] and can easily be justified for the volume imaginary potential, but its application to the imaginary surface potential is not obvious. This parametrized dependence implies that neutrons experience an equally strong asymmetry dependence as protons, but of the opposite sign, implying that neutron correlations decrease with increasing neutron excess. However, it was shown that this approach leads to inconsistencies, and it was suggested [9] that neutrons have a much smaller asymmetry dependence than protons. Other global DOM analyses have been performed, but these pertain only to positive energy data [23,24].

In order to extend our understanding of the asymmetry dependences of both proton and neutron correlations, we have extended our DOM analyses in two ways. First, for the Ca isotopes, we have made measurements of neutron elastic scattering and total reaction cross sections on ^{48}Ca. The former are discussed in Sec. II and the latter have recently been published in Ref. [25]. This work allows us to compare neutron correlations in ^{40}Ca and ^{48}Ca. Second, we have extended our analysis to include heavier closed-shell nuclei. We have obtained elastic scattering, total and reaction cross sections, and some $(e, e'p)$ data from previously published works for both protons and neutrons. The nuclei studied include the Ca, Ni, Sn, and Pb isotopes and some $N = 28$ and 50 isotones. Details of the data sets are discussed in the Appendix. A complete description of the present DOM procedure is provided in Sec. III. We have fitted the data globally in four mass regions and present the comparison with data in Sec. IV.

An important difference between the work presented here and our previous work is that we do not impose any parametrized asymmetry dependence of the imaginary surface potential such as Eq. (1) or the other form tried in our earlier work [9]. Instead, in this DOM analysis, we fit the magnitude

of this potential for each nucleus and each nucleon type separately. An analysis of the resulting potentials is performed in Sec. V. From the fitted magnitudes, we deduce the overall asymmetry dependences of the imaginary potentials in Sec. V A and the real potentials in Sec. V B. The consequences for the asymmetry dependences of the spectroscopic factors are then presented in Sec. V C. An example of the predictive power of the method is presented in Sec. VI, which discusses the behavior of occupation numbers and relies also on the work of Ref. [15] since occupation numbers are not always correctly described by the approximate expressions proposed in Ref. [14]. The example discussed in detail involves the role of neutron number on the last mostly occupied proton orbit in Sn nuclei and presents strength functions, spectroscopic factors, and occupation numbers for the $g_{9/2}$ orbit. Finally, the conclusions of this work are drawn in Sec. VII.

II. EXPERIMENT

A. Experimental method

An experiment to measure neutron elastic-scattering differential cross sections on ^{48}Ca was performed at the Triangle Universities Nuclear Laboratory (TUNL). In addition to the ^{48}Ca measurements, data were also taken with a ^{40}Ca target to compare with previous measurements and check for consistency.

The measurements were performed with the pulse-beam neutron time-of-flight technique using the ^{2}H(d,n)^{3}He reaction to produce neutrons. The experimental setup is almost the same as that described in detail by El-Kadi *et al.* [26], and so only a brief description is given here. Unpolarized deuteron beams of energies 14.4 and 9.39 MeV were extracted from the FN tandem Van de Graaff accelerator. The beams were pulsed at 2 MHz with a pulse width of 2.0 ns and had time-averaged intensities of ∼1.5 pμA. The beam traversed a 5.27-mg/cm^2 Havar foil to enter a 3.16-cm deuterium-filled gas cell that was held at 7.8 bar. The neutrons emitted from the gas cell are calculated to have mean energies of 16.9 and 11.9 MeV with energy spreads of 141 and 207 keV, respectively [27].

The target position was located 12.9 cm downstream from the center of the gas cell. The target location was enclosed in a right-cylindrical helium balloon structure of radius 7.6 cm and height 22.9 cm. The He balloon was enclosed with 840-μg/cm^2-thick Mylar, and helium at atmospheric pressure flowed throughout the measurement period. The neutrons entered the balloon at its center perpendicular to its symmetry axis. The helium helped prevent the oxidation of the Ca targets and, in addition, reduced the background in the time-of-flight spectra as the probability of neutron scattering in the helium surrounding the target is significantly reduced compared to that obtained with air.

The targets were of cylindrical geometry with a diameter of 12.7 mm and a height of ∼12 mm. Both the target and the balloon axes were aligned vertically. A natural Ca and an enriched ^{48}Ca target with masses of 2.575 and 2.717 g, respectively, were used in the measurements. The enriched target was 92.8% ^{48}Ca by atom and the only significant contaminant of the enriched target was ^{40}Ca. To reduce

the probability of oxidation during the transfer to and from the He balloon, these targets were enclosed in close-fitting argon-filled Mylar bags of wall thickness 840 μg/cm^2. These bags were positioned in the center of the balloon using thin threads. For background subtraction, data were also collected with an empty bag suspended, in the same manner as the targets, inside of the balloon.

Scattered neutrons were detected in two heavily shielded NE-218 liquid-scintillator detectors located in the horizontal reaction plane and at distances of 3.75 and 2.29 m from the target. The larger scattering angles were measured with the closer 2.29-m detector. Tapered copper and tungsten shadow bars were used to block neutrons emitted directly from the gas cell. A third, fixed scintillator detector was located at 10° and was used to monitor the neutron yield.

The pulse heights of the detectors were calibrated using the Compton-edge energies measured with ^{22}Na and ^{137}Cs γ-ray sources. Hardware thresholds were set at ∼60% of the value of the ^{137}Cs Compton edge.

For each event, the deposited energy (E), particle identification determined from the pulse shape PID, and time of flight were recorded. E-PID gates were used to obtain neutron γ-ray separation. For each angle-target configuration, a background spectrum was obtained with the empty bag. Normalization of this spectrum was obtained either from the monitor counter or from a beam-current integrator.

Absolute normalization of all cross sections was obtained from elastic scattering off of hydrogen. Measurements were performed with both polyethylene and carbon targets when the two detectors were located at 30°. This angle was chosen to maximize the separation of hydrogen scattering from the elastic- and inelastic-scattering peaks due to carbon. The carbon spectra were subtracted from the polyethylene results to yield the spectra for hydrogen scattering. The absolute normalization was obtained from the hydrogen scattering yields using the n+p cross sections given in Ref. [28].

B. Results

An example of a typical neutron time-of-flight spectrum obtained with the ^{48}Ca target and the corresponding background spectrum obtained with the empty bag is shown in Fig. 1(a) for $\theta_{\text{lab}} = 120°$. The difference between these two spectra gives the contribution from scattering by the ^{48}Ca sample and this is shown in Fig. 1(b). The arrows indicate the expected centroids for elastic scattering for $A = 12$, 16, 40, and 48 target nuclei. We observe only one significant peak, which corresponds to scattering from Ca. The yield from the small ^{40}Ca contaminant of the ^{48}Ca sample is not separable in the data. There is no measurable yield for scattering from carbon or oxygen that are found in the Mylar bag. No evidence was found for increased oxygen loading with time as one would have expected if there was significant oxidation of the targets during the experiment. The contribution of ^{40}Ca was removed using known cross sections [29,30]. For smaller angles, the Ca peak and any oxygen peak would not be completely resolved. In these cases, the elastic peak was fit with two Gaussians, one representing the contribution of ^{48}Ca and the other ^{16}O, with constrained
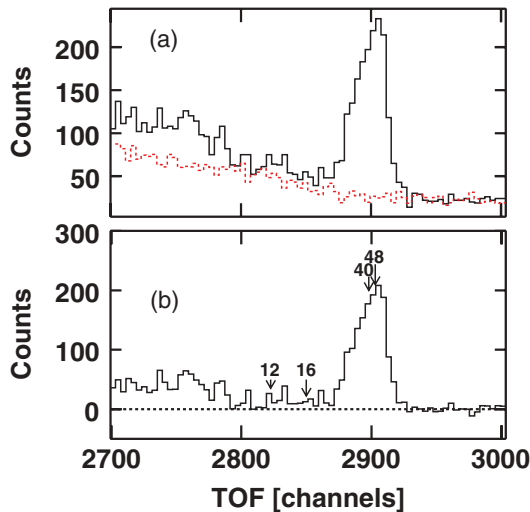
FIG. 1. (Color online) (a) Time-of-flight spectra obtained with 16.9-MeV neutrons at $\theta_{lab} = 120°$ with the ^{48}Ca target (solid histogram) and with the empty bag (dashed-histogram) by the detector located at 3.75 m. (b) The spectrum after subtraction giving the contribution from scattering by the ^{48}Ca sample. The expected centroids of scattering from the indicated target masses are shown by the arrows.

widths and centroids. The oxygen contribution was found to be always less than 1%.

All time-of-flight spectra were determined with a software threshold on the pulse height of the neutron detector of 2 and 2.2 times the value measured for the ^{137}Cs Compton edge for the 3.75- and 2.29-cm detectors, respectively. These counts were then corrected for the energy-dependent efficiency of the detector using the efficiency curves derived in Ref. [27].

To correct the data for multiple scattering in the target and the target's finite size, the experiment was simulated with the transport code GEANT4 [31]. In these simulations, the distance a deuteron projectile traveled in the 3-cm-long gas cell before reacting with the deuterium gas particle was distributed linearly. The neutron energy is linearly dependent on the distance the deuteron traveled, ranging from 16.759 to 17.041 MeV, or from 11.793 to 12.207 MeV, with the larger energy corresponding to a reaction at the back of the gas cell. The spatial distribution of the neutrons, in the axes other than the beam axis, was assumed to be Gaussian with a full width at half maximum (FWHM) of 5 mm. The angular distributions of the neutrons emitted from the gas cell is basically flat over the $\pm 5°$ region of interest for which interactions with the target are possible [32]. Thus, the initial direction of the neutrons was chosen isotropically in this interval. The neutrons then propagated in a straight line until they entered the target. The probability of scattering off a ^{48}Ca target nuclei was proportional to the length of the chord segment the neutrons passed through in the target. After scattering, the neutrons propagated in straight lines and, if they arrived at a detector, a hit was registered. The assumed $n + ^{48}$Ca differential cross sections were taken from optical-model fits to the raw experimental angular distributions.

The absolute normalization of the finite-size correction was achieved by normalizing the simulated differential cross section to the raw value at an angle where the differential cross section was relatively flat and, thus, only an insignificant finite-size correction is expected. For the 11.9-MeV data, this angle was taken to be 110°, while for the 16.9-MeV data, we selected 50° and 80° for the 2.29- and 3.75-m detectors, respectively. As expected, the finite-size corrections were by far the most significant for the sharp minima in the differential cross section. Finite-size effects fill in these minima, making them shallower and less sharp.

The corrections for finite size at 11.9 MeV were relatively small because there were no sharp minima in the differential cross sections. These corrections were at most 6%, while the average correction was approximately 1%. The finite-size corrections at 16.9 MeV were more significant; the correction in the sharp minimum was 14%. The corrections at other angles were much smaller, around 1%–3%.

The finite-size-corrected differential cross sections were fit with the optical model and the total elastic cross section was deduced. The GEANT4 simulations were then performed using this cross section to determine the scattering and multiscattering probabilities. The correction factor was then determined from the fraction of events in the simulated detector, which originated from a multiscattering interaction in the target. In the end, the effects of multiscattering were found to be quite small. The largest correction was 1.5%, and most corrections were under 0.5%. The corrections are substantially smaller than for previous neutron elastic-scattering works [29,30], as our target was significantly smaller in size.

The results obtained for ^{40}Ca are compared in Fig. 2 to previous angular distributions measured with the same apparatus [29,30]. The present results are quite consistent with the earlier measurements, with the largest deviations being ~10%.
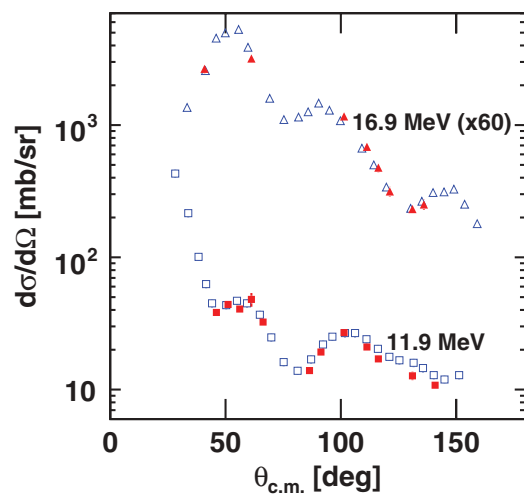
FIG. 2. (Color online) Comparison of $n + ^{40}$Ca differential cross sections measured in this work for neutron energies of 16.9 and 11.9 MeV (filled data points) to those by Honore *et al.* at 16.9 MeV [30] and Tornow *et al.* at 11.9 MeV [29] (open data points). The 16.9-MeV data have been scaled by the indicated factor.

III. DISPERSIVE-OPTICAL-MODEL ANALYSIS

A. Model description

A complete description of the dispersive optical model developed by Mahaux and Sartor can be found in Ref. [14]. The real part of the nucleon self-energy or optical-model potential can be decomposed into an energy-independent nonlocal part and an energy-dependent part, which can also be nonlocal, i.e.,

$$\text{Re}\Sigma(\boldsymbol{r}, \boldsymbol{r}'; E) = \text{Re}\Sigma(\boldsymbol{r}, \boldsymbol{r}'; E_F) + \Delta\mathcal{V}(\boldsymbol{r}, \boldsymbol{r}'; E), \qquad (2)$$

where E_F is the Fermi energy and the second term, the dispersive correction, can be determined from the imaginary part through the subtracted dispersion relation

$$\Delta\mathcal{V}(\boldsymbol{r}, \boldsymbol{r}'; E) = +\frac{1}{\pi}\mathcal{P}\int \text{Im}\Sigma(\boldsymbol{r}, \boldsymbol{r}'; E')$$
$$\times \left(\frac{1}{E' - E} - \frac{1}{E' - E_F}\right)dE', \qquad (3)$$

where $\mathcal{P}$ stands for the principal value and we note the convention to employ the same sign for the imaginary part of the self-energy above and below the Fermi energy [14]. By definition in Eq. (2), the dispersive correction is zero at the Fermi energy. The dispersive correction varies rapidly around E_F and causes the valence single-particle levels to be focused toward the Fermi energy.

Following Perey and Buck [33], the nonlocal energy-independent term $\text{Re}\Sigma(\boldsymbol{r}, \boldsymbol{r}'; E_F)$ can be approximated by a local energy-dependent term, which Mahaux and Sartor designate as the Hartree-Fock potential $\mathcal{V}_{\text{HF}}(r, E)$. Strictly, this is not a Hartree-Fock potential, but it does describe the effects of the mean field. The energy derivative of $\mathcal{V}_{\text{HF}}$ is a measure of nonlocality, which is related to the momentum-dependent effective mass

$$\frac{\widetilde{m}(r, E)}{m} = 1 - \frac{d\mathcal{V}_{\text{HF}}(r, E)}{dE}, \qquad (4)$$

where m is the nucleon mass.

A consequence of the local approximation is that one needs to use a scaled imaginary potential

$$\mathcal{W} = \frac{\widetilde{m}(r, E)}{m}\text{Im}\,\Sigma \qquad (5)$$

and a similarly scaled dispersive correction. The imaginary part of the self-energy is also approximated as a local potential and, thus, the dispersive correction is correspondingly local. Mahaux and Sartor argue that this modifies $\Delta\mathcal{V}$ by a smooth function of energy, which can easily be compensated by correspondingly smooth modification of $\mathcal{V}_{\text{HF}}$.

The Fermi energy is defined as

$$E_F = \frac{E_F{}^+ + E_F{}^-}{2}, \qquad (6)$$

$$E_F{}^+ = M_{A+1} - (M_A + m), \qquad (7)$$

$$E_F{}^- = M_A - (M_{A-1} + m), \qquad (8)$$

where $E_F{}^+$ and $E_F{}^-$ represent the binding energy for adding or removing a nucleon, or alternatively, the single-particle energies of the valence particle and hole states.

In addition to the momentum-dependent effective mass, two other effective masses can be defined. The total effective mass is given by

$$\frac{m^*(r, E)}{m} = 1 - \frac{d}{dE}[\mathcal{V}_{\text{HF}}(r, E) + \Delta\mathcal{V}(r, E)], \qquad (9)$$

while the energy-dependent effective mass is

$$\frac{\overline{m}(r, E)}{m} = 1 - \frac{m}{\widetilde{m}(r, E)}\frac{d\Delta\mathcal{V}(r, E)}{dE}. \qquad (10)$$

At the highest energies considered in this work, relativistic effects become relevant. We have included a corresponding lowest-order correction in solving the radial wave equation [34]

$$\left[\frac{d^2}{d\rho^2} + \left(1 - \frac{\widetilde{\Sigma}(\rho, E)}{E_{\text{tot}} - M - m} - \frac{\ell(\ell + 1)}{\rho^2}\right)\right]u(\rho) = 0 \qquad (11)$$

with $\rho = k\,r$, where $k = \frac{M}{E_{\text{tot}}}\sqrt{T(T + 2m)}$, T is the laboratory kinetic energy, E_{tot} is the total energy in the center-of-mass frame, and M is the target mass. The scaled potential is

$$\widetilde{\Sigma} = \gamma\,\Sigma, \quad \gamma = \frac{2(E_{\text{tot}} - M)}{E_{\text{tot}} - M + m}. \qquad (12)$$

If $u_{n\ell j}(r)$ are bound-state solutions to the radial wave equation, then the normalized wave functions corrected for nonlocality are given by

$$\overline{u}_{n\ell j}(r) = \sqrt{\frac{\widetilde{m}(r, E_{n\ell j})}{m}}u_{n\ell j}(r). \qquad (13)$$

In this paper, we have employed the following approximations, developed by Mahaux and Sartor [14], to determine bound-state properties. For valence states, the spectroscopic factor, relative to the independent-particle-model value, is

$$S_{n\ell j} = \int_0^\infty \overline{u}_{n\ell j}^2(r)\frac{m}{\overline{m}(r, E_{n\ell j})}dr, \qquad (14)$$

and the root-mean-square (rms) radius is

$$R_{n\ell j}^{\text{rms}} = \sqrt{\int_0^\infty \overline{u}_{n\ell j}^2(r)r^2dr}. \qquad (15)$$

For hole states, the occupation probability is approximated by

$$N_{n\ell j} = \int_0^\infty \overline{u}_{n\ell j}^2(r)\left[1 + \frac{m}{\overline{m}(r, E_{n\ell j})}\frac{1}{\pi}\right.$$
$$\times \left.\int_{E_F}^\infty \frac{\mathcal{W}(r, E')}{(E' - E_{n\ell j})^2}dE'\right]dr, \qquad (16)$$

while for particle states, the same approximation gives

$$N_{n\ell j} = -\int_0^\infty \overline{u}_{n\ell j}^2(r)\left[\frac{m}{\overline{m}(r, E_{n\ell j})}\frac{1}{\pi}\right.$$
$$\times \left.\int_{-\infty}^{E_F} \frac{\mathcal{W}(r, E')}{(E' - E_{n\ell j})^2}dE'\right]dr. \qquad (17)$$

B. Parametrization of the potentials

The parametrization of the real and imaginary optical-model potentials is the central aspect of a DOM analysis. The number of free parameters in the fits must be sufficient to allow one to describe the important physics, but not too large or fitting becomes impractical in terms of CPU usage. The functional forms we have used in the this paper are mostly similar to our previous study [9], which were based on theoretical expectations and confrontation with data, although there are some differences that are discussed below.

The imaginary potential is composed of the sum of volume, surface, and imaginary spin-orbit components

$$\mathcal{W}(r, E) = -W^{\mathrm{vol}}(E, r) + 4a^{\mathrm{sur}}W^{\mathrm{sur}}(E)$$
$$\times \frac{d}{dr} f(r, r^{\mathrm{sur}}, a^{\mathrm{sur}}) + \mathcal{W}^{\mathrm{so}}(r, E), \quad (18)$$

with Woods-Saxon form factors

$$f(r, R^i, a^i) = \frac{1}{1 + e^{\frac{r - R^i}{a^i}}}. \quad (19)$$

Standard optical-model fits to elastic-scattering data at a single energy require a surface-type absorption at low bombarding energies $E \ll 50$ MeV and a volume-type absorption at high bombarding energies $E \gg 50$ MeV. However, fits encompassing a large range of energies often have a significant, but small, surface absorption component extending to energies much larger than 50 MeV [9,21,35]. One can reconcile these statements by noting that the addition of a small surface component to a volume-type component acts to increase the radius of the volume component.

If the radius of the volume potential is increased by δR, we find, after a Taylor expansion, that

$$f(r, R + \delta R, a) \sim f(r, R, a) + \frac{df}{dR}\delta R \quad (20)$$

$$\sim f(r, R, a) - \frac{df}{dr}\delta R, \quad (21)$$

and thus the first-order correction is a surface-type component.

Thus, a gradually decaying surface term above $E = 50$ MeV can be understood as being associated with a volume-type component, the radius of which decreases with energy. Such a feature is found in the Jeukenne, Lejeune, and Mahaux potential [36,37], which is derived from infinite-matter calculations coupled with the local-density approximation to get the potential in the surface region. We have assumed the radius of the imaginary volume potential to decay with energy as

$$R^{\mathrm{vol}}(E) = R_0^{\mathrm{vol}} + \delta R \exp\left(-\frac{|E - E_F|}{E_R}\right). \quad (22)$$

However, an energy dependence of the radius was not used in the fits as it would require the dispersive correction to be calculated for each r value, which would be very CPU intensive. Instead, we make use of the expansion of Eq. (21) to obtain

$$W^{\mathrm{vol}}(E, r) = W_0^{\mathrm{vol}}(E)f(r, R_0^{\mathrm{vol}}, a^{\mathrm{vol}})$$
$$- 4a^{\mathrm{vol}}W_{\mathrm{sc}}^{\mathrm{vol}}(E)\frac{d}{dr}f(r, R_{\mathrm{sc}}^{\mathrm{vol}}, a^{\mathrm{vol}}), \quad (23)$$

where $W_0^{\mathrm{vol}}(E)$ is the energy dependence of the depth of the volume component, and the surface correction, which accounts for the energy dependence of the radius, is

$$W_{\mathrm{sc}}^{\mathrm{vol}}(E) = W_0^{\mathrm{vol}}(E)\frac{\delta R}{4a^{\mathrm{vol}}} \exp\left(-\frac{|E - E_F|}{E_R}\right). \quad (24)$$

Thus, in this paper we also have a surface component that extends well beyond $E = 50$ MeV; however, unlike other studies, it is not tied to the "true" surface component at lower energies, which is important if we are going to separate the asymmetry dependences of the surface and volume components. It is also useful to maintain a distinction between the "true" surface potential at low energies, which is associated with long-range correlations, and the surface correction at high energies, which is associated with short-range correlations.

The phase space of particle levels for $E \gg E_F$ is significantly larger than that of hole levels for $E \ll E_F$. Therefore, the contributions from two-particle–one-hole states for $E \gg E_F$ to the self-energy will be larger than that for two-hole–one-particle states at $E \ll E_F$. Thus, at energies well removed from E_F, the form of the imaginary volume potential should no longer be symmetric about E_F. Hence, the following form was assumed for the depth of the volume potential:

$$W_0^{\mathrm{vol}}(E) = \Delta W_{\mathrm{NM}}(E) + \begin{cases} 0 & \text{if } |E - E_F| < E_p^{\mathrm{vol}}, \\ A^{\mathrm{vol}}\left(1 \pm C^{\mathrm{vol}}\frac{N-Z}{A}\right)\frac{\left(|E-E_F|-E_p^{\mathrm{vol}}\right)^4}{\left(|E-E_F|-E_p^{\mathrm{vol}}\right)^4 + (B^{\mathrm{vol}})^4} & \text{if } |E - E_F| > E_p^{\mathrm{vol}}, \end{cases} \quad (25)$$

where $\Delta W_{NM}(E)$ is the energy-asymmetric correction modeled after nuclear-matter calculations. Apart from this correction, the parametrization is similar to the Jeukenne and Mahaux form [38] used in many DOM analyses. For the asymmetry term, the $+$ and $-$ values refer to protons and neutrons, respectively. This form of the asymmetry potential is consistent with the Lane potential [22] and for short-range correlations can be justified based on the difference between the *n-p* and the *n-n* or *p-p* in medium nucleon-nucleon cross sections [9]. Nuclear-matter calculations of occupation

probabilities, which should be closely associated with the volume component, also suggest that this form is valid except for extreme asymmetry values [7,8].

We set the parameter $E_p^{\mathrm{vol}} = 11$ MeV to force the imaginary potential to be zero just in the vicinity of the Fermi energy (see later). The radii of the volume and surface-correction components W_0^{vol} and $W_{\mathrm{sc}}^{\mathrm{vol}}$ are taken to be identical:

$$R_0^{\mathrm{vol}} = r_0^{\mathrm{vol}}A^{1/3}. \quad (26)$$

The energy-asymmetric correction was taken as

$$\Delta W_{NM}(E) = \begin{cases} \alpha A^{\mathrm{vol}}\left[\sqrt{E} + \frac{(E_F+E_a)^{3/2}}{2E} - \frac{3}{2}\sqrt{E_F+E_a}\right] & \text{for } E - E_F > E_a, \\ -A^{\mathrm{vol}}\frac{(E_F-E-E_a)^2}{(E_F-E-E_a)^2+(E_a)^2} & \text{for } E - E_F < -E_a, \\ 0 & \text{otherwise,} \end{cases} \quad (27)$$

which is similar to the form suggested by Mahaux and Sartor [14]. Following our previous study [9], we have taken $\alpha = 0.08$ MeV$^{-1/2}$ and $E_a = 60$ MeV. The "true" imaginary surface potential is taken to have the form

$$W^{\mathrm{sur}}(E) = \begin{cases} 0 & \text{if } |E - E_F| < E_p^{\mathrm{sur}}, \\ \frac{A^{\mathrm{sur}}}{1+\exp\left(\frac{|E-E_F|-C^{\mathrm{sur}}}{D^{\mathrm{sur}}}\right)}\frac{\exp\left(\frac{|E-E_F|-E_p^{\mathrm{sur}}}{B^{\mathrm{sur}}}\right)-1}{\exp\left(\frac{|E-E_F|-E_p^{\mathrm{sur}}}{B^{\mathrm{sur}}}\right)+1} & \text{if } |E - E_F| > E_p^{\mathrm{sur}}, \end{cases} \quad (28)$$

where, for protons and neutrons $(i = n, p)$, the $E^{\mathrm{sur}}(i)_p$ parameter is related to the experimental particle-hole energy gaps Δ_i via

$$E_p^{\mathrm{sur}(i)} = f_\Delta\left[\frac{\Delta_i}{2} + \min(\Delta_p, \Delta_n)\right], \quad (29)$$

$$\Delta_i = E_F^{(i)+} - E_F^{(i)-}. \quad (30)$$

In the independent-particle model, $f_\Delta = 1$ and E_p^{sur} represents the minimum particle energy above the Fermi value, for which a particle can couple to a two-particle–one-hole excitation. Similarly, it also characterizes the maximum energy, relative to the Fermi value, for which a hole can couple to the a two-hole–one-particle excitation. Thus, between these two limits, damping of single-particles states is not possible and the imaginary potential should exhibit a region of width $2E_p^{\mathrm{sur}}$, where it is exactly zero. Many-body correlations reduce the width of this gap and, thus, we include the fitting parameter f_Δ. Mahaux and Sartor had also explored imaginary potentials, which were zero in the immediate vicinity of the Fermi energy [14]; however, they assumed a somewhat different energy dependence.

The mass dependence was taken as

$$R^{\mathrm{sur}} = r_0^{\mathrm{sur}} A^{1/3} \quad (31)$$

and the parameter A^{sur} was individually fit for each nucleus and nucleon type.

The Hartree-Fock potential is parametrized in the following way:

$$\mathcal{V}_{\mathrm{HF}}(r, E) = -V_{\mathrm{HF}}^{\mathrm{vol}}(E)\,f(r, r^{\mathrm{HF}}, a^{\mathrm{HF}}) + 4V_{\mathrm{HF}}^{\mathrm{sur}}\frac{d}{dr}$$
$$\times f(r, r^{\mathrm{HF}}, a^{\mathrm{HF}}) + V_c(r) + \mathcal{V}^{\mathrm{so}}(r, E), \quad (32)$$

where the Coulomb V_C and real spin-orbit $\mathcal{V}^{\mathrm{so}}$ terms have been separated from the volume and surface components. The volume component contains the energy dependence representing nonlocality, which is approximated by the cubic equation

$$V_{\mathrm{vol}}^{\mathrm{HF}}(E) = V_0^{\mathrm{HF}} - \alpha^{\mathrm{vol}}(E - E_F) - \beta^{\mathrm{vol}}(E - E_F)^2$$
$$- \gamma^{\mathrm{vol}}(E - E_F)^3. \quad (33)$$

The value of V_0^{HF} is constrained for each nucleus and nucleon type by obtaining the correct Fermi energy. This is essentially independent of the imaginary potential and their dispersive corrections, i.e., the dispersive corrections have equal but opposite effects on E_F^+ and E_F^- and so cancel in the calculation of the Fermi energy in Eq. (6). We have included an asymmetry dependence of α^{vol}:

$$\alpha^{\mathrm{vol}} = \alpha_0^{\mathrm{vol}} \pm \alpha_{NZ}^{\mathrm{vol}}\frac{N - Z}{A} \quad (34)$$

and

$$R^{\mathrm{HF}} = r_0^{\mathrm{HF}} A^{1/3}. \quad (35)$$

The Hartree-Fock surface component was found necessary to fit high-energy elastic-scattering data [9] and was parametrized as

$$V_{\mathrm{HF}}^{\mathrm{sur}}(E) = \begin{cases} 0 & \text{if } x < 0, \\ \alpha^{\mathrm{sur}}\frac{x^2}{x^2+(\gamma^{\mathrm{sur}})^2} & \text{if } x > 0, \end{cases} \quad (36)$$

where

$$x = E - E_F - \beta^{\mathrm{sur}}. \quad (37)$$

The Coulomb potential was taken as that of a sharp-surfaced sphere with radius

$$R_C = r_C A^{1/3}. \quad (38)$$

At high energies, OM potentials generally include an imaginary spin-orbit potential [39]. Given that this term is usually assumed to be zero for lower energies, this implies that the imaginary spin-orbit term is energy dependent. As such, it should give rise to a dispersive correction to the real component. Given these considerations, the total spin-orbit potential was taken as

$$\mathcal{U}^{\mathrm{so}}(r, E) = \mathcal{V}^{\mathrm{so}}(r, E) + i\mathcal{W}^{\mathrm{so}}(r, E)$$
$$= \Delta\mathcal{V}^{\mathrm{so}}(r, E) + \left(\frac{h}{m_\pi c}\right)^2 [V^{\mathrm{so}} + i W^{\mathrm{so}}(E)]$$
$$\times \frac{1}{r}\frac{d}{dr}f(r, R^{\mathrm{so}}, a^{\mathrm{so}})\frac{\boldsymbol{\ell}\cdot\boldsymbol{s}}{2},$$

where $(\hbar/m_\pi c)^2 = 2.0$ fm^2 and $\Delta\mathcal{V}^{\mathrm{so}}$ is the dispersive correction determined from the imaginary component $\mathcal{W}^{\mathrm{so}}$. As the imaginary spin-orbit component is generally needed only at

TABLE I. Fitted and fixed parameter values obtained in this paper for the four indicated fit regions. For entries indicated by a fix, the quantity was fixed during the fits. For those indicated by an asterisk, a single value, which was taken from the average of initial individual fits, is used for all fitting regions. The table also contains the number of the equation that defines each individual parameter.

	$Z = 20, 28,$ $N = 28$	$N = 50$	$Z = 50$	$Z = 82$	Eq.
r_C (fm)	1.3(fix)	1.3(fix)	1.3(fix)	1.3(fix)	(38)
α_0^{vol}	0.51	0.47	0.42	0.38	(34)
$\alpha_{NZ}^{\mathrm{vol}}$	0.16	0.14(fix)	0.14(fix)	0.13	(34)
β^{vol} (10^{-4} MeV^{-1})	-6.7	-10.5	-6.9(fix)	-7.1	(33)
γ^{vol} (10^{-6} MeV^{-2})	-1.8	-0.7(fix)	0(fix)	0.6	(33)
α^{sur} (MeV)	7.64	6.17	7.42(fix)	7.21	(36)
β^{sur} (MeV)	7.17	8.00	14.2(fix)	21.2	(37)
γ^{sur} (MeV)	63.9	82.7	92(fix)	121	(36)
r_0^{HF} (fm)	1.18	1.21	1.24	1.23	(35)
a^{HF} (fm)	0.65	.62	0.75	0.70	(19)
f_Δ	0.8(*)	0.8(8)	0.8(*)	0.8(*)	(29)
B^{sur} (MeV)	10.0	7.0	8.3	15.0	(28)
C^{sur}	33.6	46.8	37.2	30.4	(28)
D^{sur}	12.2	7.1	10.9	11.5	(28)
r_0^{sur} (fm)	1.17	1.13	1.20	1.20	(31)
a^{sur} (fm)	0.6(fix)	0.6(fix)	0.6(fix)	0.6(fix)	(19)
A^{vol} (MeV)	7.94	8.63	8.50(fix)	9.07	(25)
C^{vol}	4.22(fix)	4.22(fix)	4.22(fix)	4.22	(25)
B^{vol} (MeV)	40.0	41.2	43.7	40.8	(25)
r_0^{vol} (fm)	1.35	1.28	1.33	1.28	(26)
δR [fm]	2.38	3.22	4.00	4.60	(24)
a^{vol} (fm)	0.6(fix)	0.6(fix)	0.6(fix)	0.6(fix)	(19)
E_R (MeV)	35.5(*)	35.5	35.5(*)	35.5(*)	(24)
α (MeV$^{-1/2}$)	0.08(fix)	0.08(fix)	0.08(fix)	0.08(fix)	(27)
E_a (MeV)	60(fix)	60(fix)	60(fix)	60(fix)	(27)
E_p^{vol} (MeV)	11(fix)	11(fix)	11(fix)	11(fix)	(25)
V_0^{so} (MeV)	6.37	5.71	6.32	6.07	(40)
V_{NZ}^{so} (MeV)	-1.31(*)	-1.31(*)	-1.31(*)	-1.31(*)	(40)
r_0^{so} (fm)	0.98	1.00	1.11	1.11	(41)
a^{so} (fm)	0.70(*)	0.70(*)	0.7(*)	0.7(*)	(19)
A^{so} (MeV)	-3.65(*)	-3.65(*)	-3.65(*)	-3.65	(39)
B^{so} (MeV)	208(*)	208(*)	208(*)	208(*)	(39)

high energies, we choose the form

$$W^{\mathrm{so}}(E) = A^{\mathrm{so}} \frac{(E - E_F)^4}{(E - E_F)^4 + (B^{\mathrm{so}})^4}. \qquad (39)$$

The dispersive correction $\Delta \mathcal{V}^{\mathrm{so}}(E)$ associated with this component gives an approximately linear decrease in magnitude of the total real spin-orbit strength over the energy region of interest. The mass and asymmetry dependences of the spin-orbit potential were taken as

$$V^{\mathrm{so}} = V_0^{\mathrm{so}} \pm V_{NZ}^{\mathrm{so}} \frac{N - Z}{A}, \qquad (40)$$

$$R^{\mathrm{so}} = r_0^{\mathrm{so}} A^{1/3}. \qquad (41)$$

IV. RESULTS OF FITS

Global fits to elastic-scattering data, total and reaction cross sections, single-particle energies, rms radii, and spectroscopic factors were performed for four regions: (1) Ca, Ni isotopes and $N = 28$ isotones, (2) $N = 50$ isotones, (3) Sn isotopes, and (4) ^{208}Pb. The data sets and their references are listed in the Appendix . The final fitted parameters for these four regions are listed in Tables I and II. The fitted elastic-scattering differential cross sections are shown in Figs. 3–5 and the fitted analyzing powers are displayed in Figs. 6 and 7. Fitted reaction cross sections for protons are shown in Fig. 8, while fitted reaction and total cross sections for neutrons can be found in Fig. 9. The relative difference in total neutron cross sections between ^{40}Ca and ^{48}Ca was also included in the fitting, and the fitted results are displayed in Fig. 10. The quality of the fits are at least as good, if not better, than other global optical-model fits.

In the final fits, constraints on some parameters were made based on initial fits. In a number of cases, a fitted parameter was similar in the four fit regions. In some cases, we attempted to replace these values by an average value from the four fit regions and, if in the subsequent refit, the χ^2 didn't increase significantly, then the average value was kept. These values are indicated by the asterisk symbols in Table I.

TABLE II. The Fermi energy and fitted values of the magnitudes of the Hartree-Fock and imaginary surface potentials and the maximum of the imaginary surface potential for all the nuclei studied.

System	E_F (MeV)	V_0^{HF} (MeV)	A^{sur} (MeV)	W_{max}^{sur} (MeV)
$p+^{40}$Ca	−4.7	59.2	14.6	6.7
$p+^{42}$Ca	−7.6	61.9	18.5	9.4
$p+^{44}$Ca	−9.5	63.0	19.6	9.9
$p+^{48}$Ca	−13.2	64.8	19.1	9.4
$p+^{50}$Ti	−10.1	65.9	20.7	10.6
$p+^{52}$Cr	−8.5	63.3	16.8	8.6
$p+^{54}$Fe	−7.0	60.7	15.1	7.8
$p+^{58}$Ni	−5.8	60.8	16.4	8.5
$p+^{60}$Ni	−7.2	61.8	17.8	9.1
$p+^{62}$Ni	−8.6	62.8	19.2	9.8
$p+^{64}$Ni	−10.0	63.8	18.2	9.3
$p+^{90}$Zr	−6.8	59.3	9.95	8.7
$p+^{92}$Mo	−5.8	60.1	13.1	11.4
$p+^{112}$Sn	−5.3	59.9	16.9	10.6
$p+^{114}$Sn	−6.1	59.5	18.0	11.4
$p+^{116}$Sn	−6.8	60.0	21.0	13.4
$p+^{118}$Sn	−7.6	60.4	22.2	14.2
$p+^{120}$Sn	−8.2	60.8	26.2	16.7
$p+^{122}$Sn	−9.0	61.4	25.4	16.3
$p+^{124}$Sn	−9.7	61.8	28.2	18.1
$p+^{208}$Pb	−5.9	61.2	35.7	13.1
$n+^{40}$Ca	−12.0	58.7	15.6	7.1
$n+^{48}$Ca	−7.5	54.1	14.2	7.1
$n+^{54}$Fe	−11.3	56.8	15.5	8.0
$n+^{58}$Ni	−10.6	57.0	16.0	8.4
$n+^{60}$Ni	−9.6	56.1	16.3	8.5
$n+^{92}$Mo	−10.3	53.3	10.8	9.4
$n+^{116}$Sn	−8.3	48.8	13.2	8.6
$n+^{118}$Sn	−7.6	47.2	12.9	8.4
$n+^{120}$Sn	−7.6	47.3	12.8	8.3
$n+^{124}$Sn	−7.1	48.8	12.6	8.2
$n+^{208}$Pb	−5.6	47.1	21.6	8.0

In other cases, a parameter could not be adequately constrained from the available data. This is especially true for the Sn region where there is a lack of high-energy data to constrain the imaginary volume potential and the higher-order energy dependence of the Hartree-Fock potentials. In such cases, an intermediate value between the neighboring regions was chosen and fixed in the fits. Such cases are indicated by a fix in Table I. Also, the parameters r_C, a^{vol}, and a^{sur} were fixed at reasonable values to reduce the number of fitting parameters.

A perusal of the remaining parameters generally reveals a consistency between the fits. The parameters a^{HF}, r^{sur}, A^{vol}, B^{vol}, V_0^{so}, and r^{so} are quite similar in the different fit regions. The parameters α_0^{vol}, r^{HF}, and δR show systematic mass dependences. The value of $\delta R = 4.60$ fm for the Pb region may seem large, but over the energy region where the volume imaginary potential is significant in our fits (B^{vol} to 200 MeV), the radius of W^{vol} changes by only 1.45 fm.

The spectroscopic factors and rms radii derived from $(e, e'p)$ measurements on ^{40}Ca, ^{48}Ca, ^{90}Zr, and ^{208}Pb are compared to the fitted values in Figs. 11 and 12. The rms

radii are well fit and put tight constraints of the values of r^{HF} and a^{HF}. The fitted spectroscopic factors for the Ca isotopes are a little too high, approximately twice the experimental σ values away from, but still consistent with, the experimental values.

Finally, fitted single-particle energies $E_{n\ell j}$ are shown in Figs. 13–15. For levels well below the Fermi energy, the single-particle strength is highly fragmented and the plotted values represent the mean energy. In Fig. 13, the A dependence of some single-particle levels is presented. Quite generally, the energies of the valence hole and particle states in the immediate vicinity to the Fermi energy are well described. The more deeply bound proton levels ($0d_{5/2}$, $1s_{1/2}$, $0d_{3/2}$) for the Ni isotopes in Fig 13(b) are not well reproduced. These levels have a greater experimental uncertainty concerning the average location of the level strength. There may be even more deeply bound strength unaccounted for in the experiments, biasing the quoted result to higher energies. However, the tensor force, which is not explicitly included in our fits, may well be responsible for the behavior of the experimental data [40]. Also, in Fig. 13(a), one observes that the trend in the $0d_{3/2}$ proton levels in the Ca isotopes is not a smooth linear function of A as in the fits. Again, this might be a consequence of the influence of the tensor interaction.

For the ^{40}Ca and ^{58}Ni systems, the average strength of the deeply bound $0s_{1/2}$ and $0p$ proton levels is known. These are compared to the fitted values in Fig. 14. The location of this strength is described in the fits as well as the shallower levels. Finally, in Fig. 15, the levels in the vicinity of the Fermi energy for the double closed-shell nuclei ^{40}Ca, ^{48}Ca, and ^{208}Pb are compared to the fitted values. The reproduction is adequate, but certainly not perfect.

V. ANALYSIS OF FITTED POTENTIALS

A. Asymmetry dependences

From the asymmetry dependences of the imaginary potentials, one can infer the asymmetry dependence of the spectroscopic factors, occupation probabilities, and determine how nucleon correlations change with increasing neutron or proton richness. Examples of the fitted energy dependences of the magnitudes of the imaginary potentials for some Ca, Sn, and Pb isotopes are shown in Fig. 16. Both the surface [$W^{sur}(E)$, Eq. (28)] and volume [$W_0^{vol}(E)$, Eq. (25)] components for both protons (solid curves) and neutrons (dashed curves) are shown.

The magnitude of the asymmetry dependence of the imaginary volume potential can be gauged by the differences between the proton and neutron volume components in each panel of Fig. 16. For the $N = Z$ ^{40}Ca nucleus in Fig. 16(d), the neutron and proton volume potentials are identical by definition [Eq. (25)]. The magnitude of the asymmetry coefficient C^{vol} in Eq. (25) was determined solely from the ^{208}Pb data and applied to all other fits. The ^{208}Pb data is the most appropriate for determining C^{vol} as ^{208}Pb has the largest asymmetry of all systems studied and has significant data for both neutrons and protons at energies above 50 MeV where the volume absorption is dominant. The magnitude of C^{vol}
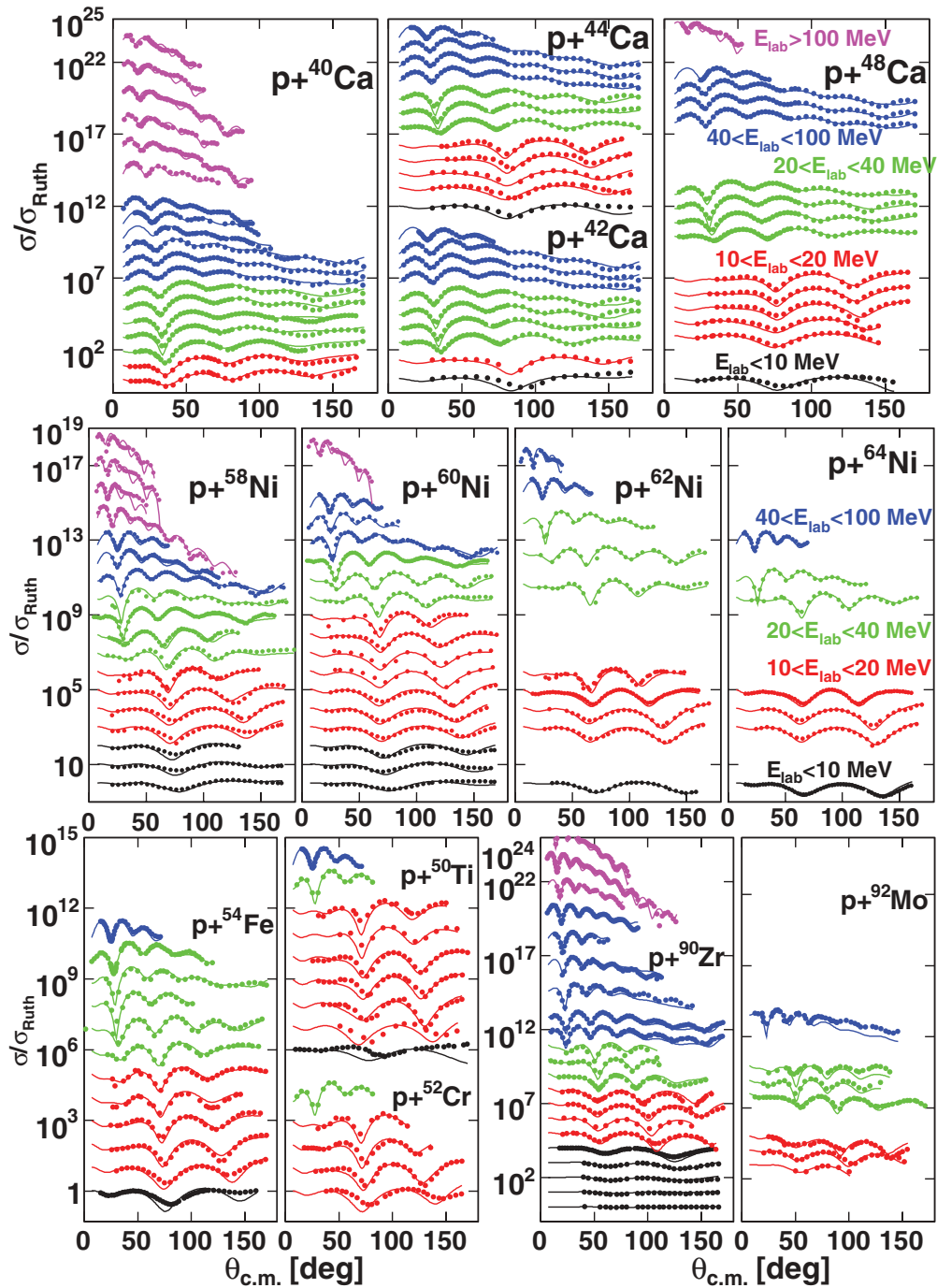
FIG. 3. (Color online) Fitted proton elastic-scattering differential cross sections expressed as a ratio to the Rutherford scattering value. Data from each energy are offset along the vertical axis for clarity. Lowest energy on the bottom and highest energy on the top for each frame. Individual energies can be obtained from Tables IV–VIII.

is directly related to the difference between the proton and neutron volume potentials in each of the panels of Fig. 16.

The other quantities A^{vol} and B^{vol}, parametrizing the volume potential in Eq. (25), were fit individually for the ($Z = 20$, 28 and $N = 28$) and Pb regions. These values listed in Table I are quite consistent. Their average value was imposed on the fits to the Sn and $N = 50$ regions where there is little higher-energy data to constrain them.

The asymmetry dependence of the volume component, undoubtedly associated with the tensor interaction, is quite modest. On the other hand, we see in Fig. 16 very strong increases in the proton surface component with increasing neutron number in the Ca and Sn isotopes. Also, we see very large differences in the surface component between protons and neutrons for all but the ^{40}Ca case. In this instance, unlike the volume case, the agreement between the magnitudes of proton and neutron
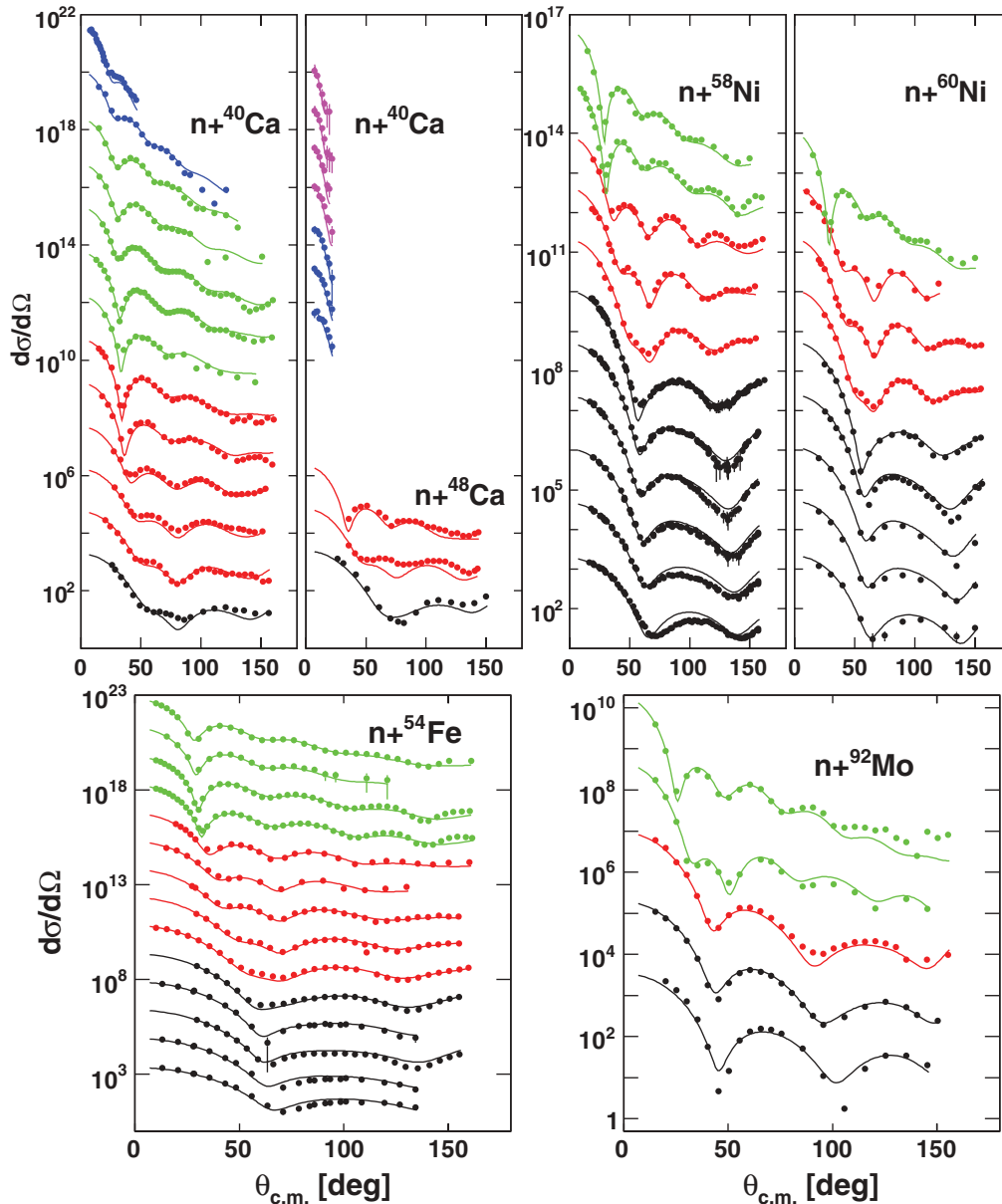
FIG. 4. (Color online) Fitted neutron elastic-scattering differential cross sections for reactions on Ca, Ni isotopes, and ^{54}Fe and ^{92}Mo. Data from each energy are offset along the vertical axis for clarity. Lowest energy on the bottom and highest energy on the top for each frame. Individual energies can be obtained from Tables V–VIII.

imaginary surface potential for ^{40}Ca is not forced, but a result of the fit. The neutron imaginary potentials show only small dependences on A and asymmetry unlike the protons.

The asymmetry dependence of the W_{max}^{sur}, the maximum value of the magnitude of the imaginary surface potential $W^{sur}(E)$, is plotted for all Sn isotopes studied in Fig. 17. These maximum values for protons show a substantial increase with $(N - Z)/A$, whereas for neutrons there is almost no change. The proton data could be well fit by a linear relationship; however, a linear extrapolation to ^{100}Sn [$(N - Z = 0)/A$] would give a value of W_{max}^{sur} close to zero. This seems unlikely and suggests that the true asymmetry dependence is nonlinear.

The asymmetry dependence for the $Z = 20$, 28 and $N = 28$ fits are shown in Fig. 18. Here, the asymmetry dependences are

more complicated than those obtained for the Sn isotopes. For protons, we see an initial increase with increasing asymmetry, but, subsequently, the magnitude of the W_{max}^{sur} saturates at around 10 MeV. For neutrons, we also see an initial increase with asymmetry, but for ^{48}Ca, the data point with the maximum value of asymmetry W_{max}^{sur} is almost identical to its value for ^{40}Ca, the data point with the minimum asymmetry. This may suggest an initial rise and then fall of W_{max}^{sur} with asymmetry, but the number of data points is small and, thus, this generalization may be premature.

In fact, it is not clear that an asymmetry parameter is the most appropriate one to characterize the neutron dependences. In Fig. 19, W_{max}^{sur} is plotted as a function of proton number Z for all the neutron cases studied. Here, we see that the magnitude of
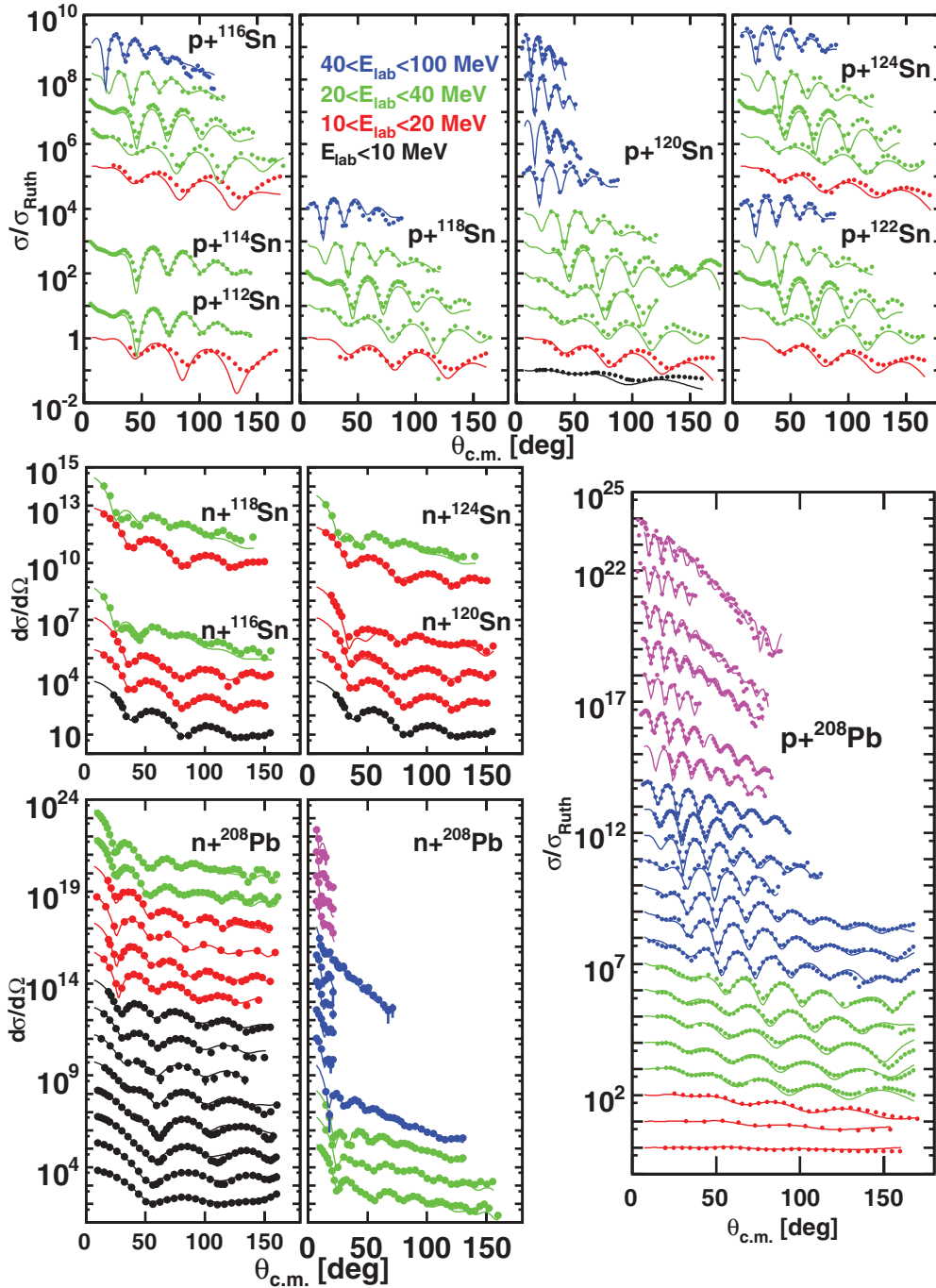
FIG. 5. (Color online) Fitted elastic-scattering differential cross sections for proton and neutron reactions on Sn isotopes and ^{208}Pb. Data from each energy are offset along the vertical axis for clarity. Lowest energy on the bottom and highest energy on the top for each frame. Individual energies can be obtained from Tables IX and X.

the imaginary surface potential for neutrons is very similar for all cases studied and only varies by 20%. Also, the data points with the same Z values almost completely overlap, suggesting that, for neutrons, this may be a better way to extrapolate $W_{\max}^{\rm sur}$ values. For protons, plotting $W_{\max}^{\rm sur}$ versus either Z or N does not add new insight.

The stronger asymmetry dependence obtained for protons can also be deduced more directly from some of the data sets.

In standard optical-model fits to an angular distribution from a single-proton energy, there is often no unique fit. However, the volume integral of the potentials is generally found to be similar for all good fits [41]. The magnitude of the integrated imaginary potential

$$J_W(E) = \int d\mathbf{r}\, W(\mathbf{r}, E) \tag{42}$$
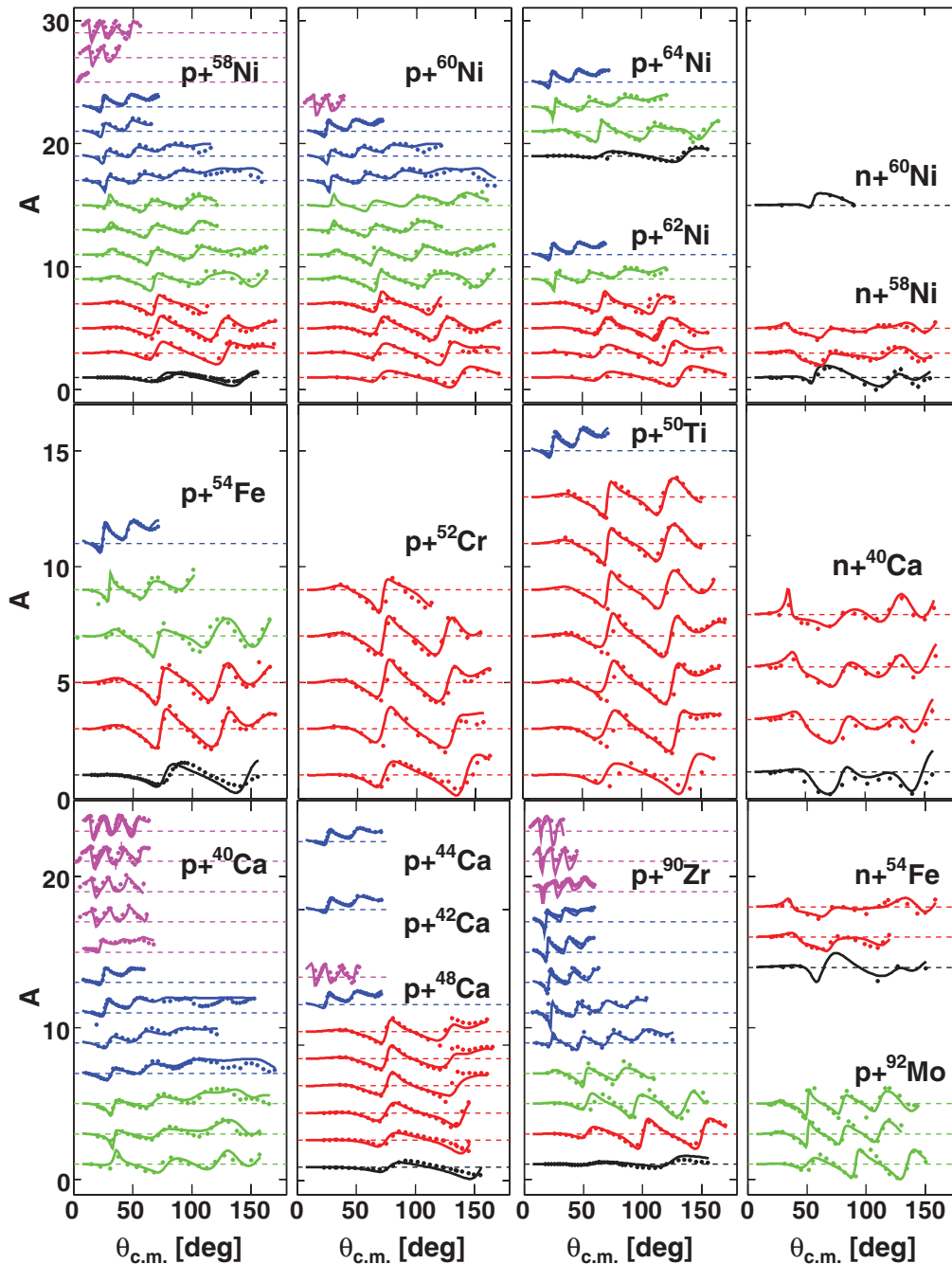
FIG. 6. (Color online) Fitted analyzing powers for proton and neutron reactions on $Z = 20$, 28 and $N = 28$, 50 target nuclei. For clarity, successively larger energies have been shifted further up along the vertical axis. The dashed lines indicate zero analyzing power for each energy.

for ~20 MeV protons in Sn and Ca isotopes obtained by Wassenaar *et al.* [42] and McCamis *et al.* [43] is plotted as a function of A in Figs. 20(a) and 21(a). The data have been scaled by A^{-1} to remove the effect of increasing volume with increasing A. At 20 MeV, the results are dominated by the imaginary surface potential and the deduced dependences are similar to the extracted asymmetry dependence of W_{max}^{sur} in Figs. 17 and 18, i.e., with increasing neutron number, the magnitude of the imaginary surface potential increases for Sn isotopes. For Ca isotopes, there is an initial increase and a

subsequent saturation of the imaginary potential as seen in the extracted W_{max}^{sur} in Fig. 18.

Similar trends can also be observed in the proton reaction cross sections. Figures 20(b) and 21(b) show the A dependence of the reaction cross sections scaled by $A^{-2/3}$ to take into account the change in radius. The results for proton energies of 25 MeV, which again emphasize the imaginary surface component, were obtained by Carlson *et al.* [44,45]. These figures also display the same trends as found for $|J_W|/A$ and W_{max}^{sur}. The elastic-scattering and reaction cross-section
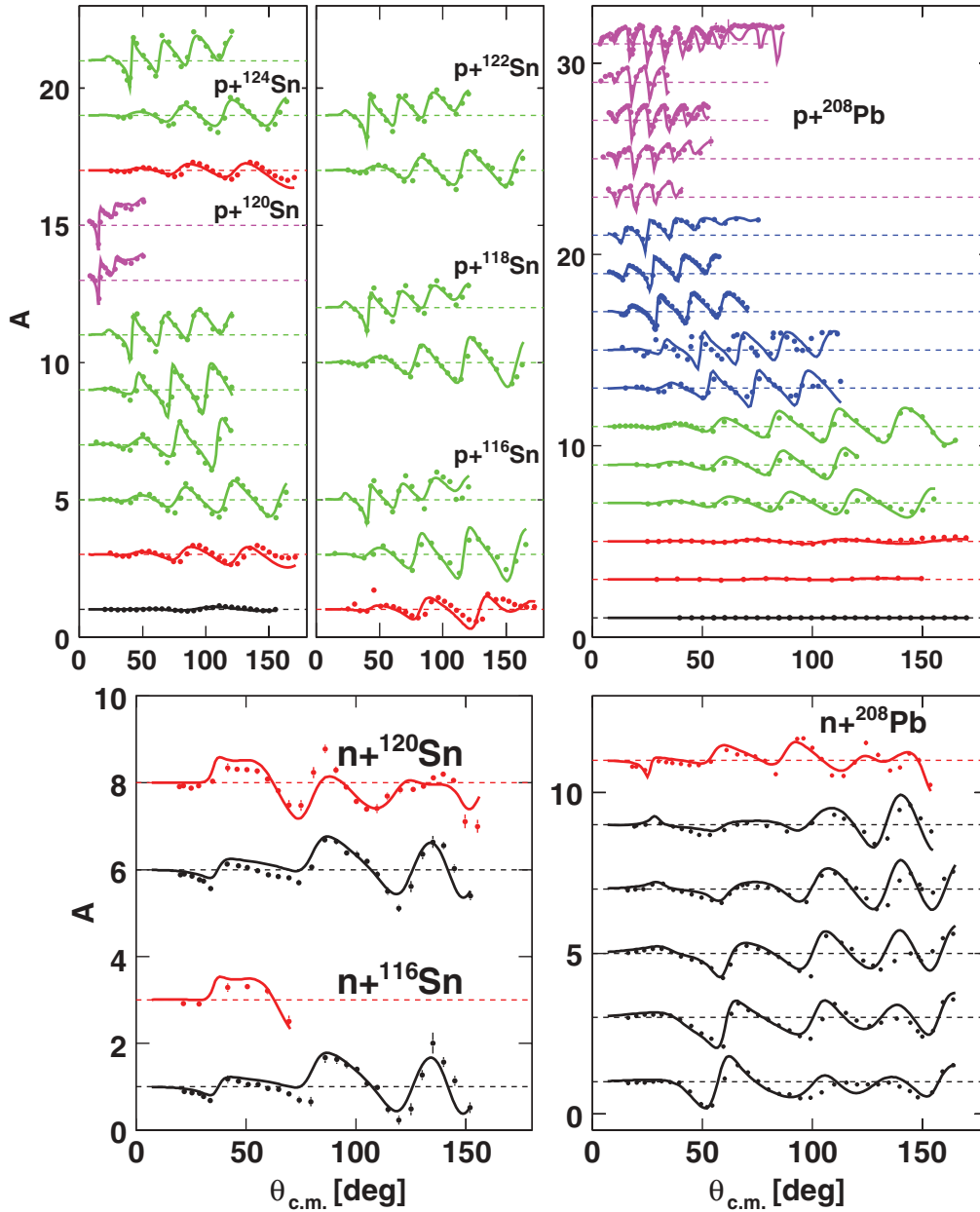
FIG. 7. (Color online) As for Fig. 6, but reactions on Sn isotopes and ^{208}Pb.

data thus present consistent pictures of the asymmetry dependence.

For the $N = 50$ region, we only have data for two nuclei and thus are not able to draw conclusions about the overall asymmetry dependence. We note that, in Table II, the $p+^{92}$Mo value of $W_{\mathrm{max}}^{\mathrm{sur}}$ is 30% larger than the $p+^{90}$Zr values. In this case, the system with the larger neutron-proton asymmetry has the smaller value $W_{\mathrm{max}}^{\mathrm{sur}}$. Possibly this is a local fluctuation, but more data are needed for other $N = 50$ isotones to draw any firm conclusions.

B. Real potential

The magnitude of the real Hartree-Fock potential was determined individually for each nucleus and nucleon type

by requiring the correct Fermi energy. This procedure is independent of the magnitude of the imaginary potentials. A typical parametrization of the magnitude of the real nuclear potential in standard optical-model fits is [20]

$$V^{\mathrm{OM}}(E) = V_0^{\mathrm{OM}} \pm V_1^{\mathrm{OM}} \frac{N - Z}{A} - \alpha^{\mathrm{vol}}(E - \overline{V_C}), \quad (43)$$

where the average Coulomb energy of the nucleon inside of the nucleus is given by

$$\overline{V_C} = \frac{1.73 \, Z Z_N}{R_C}, \quad (44)$$

and Z_N is the atomic number of the nucleon. This form is consistent with the Lane potential [22] and the second term is
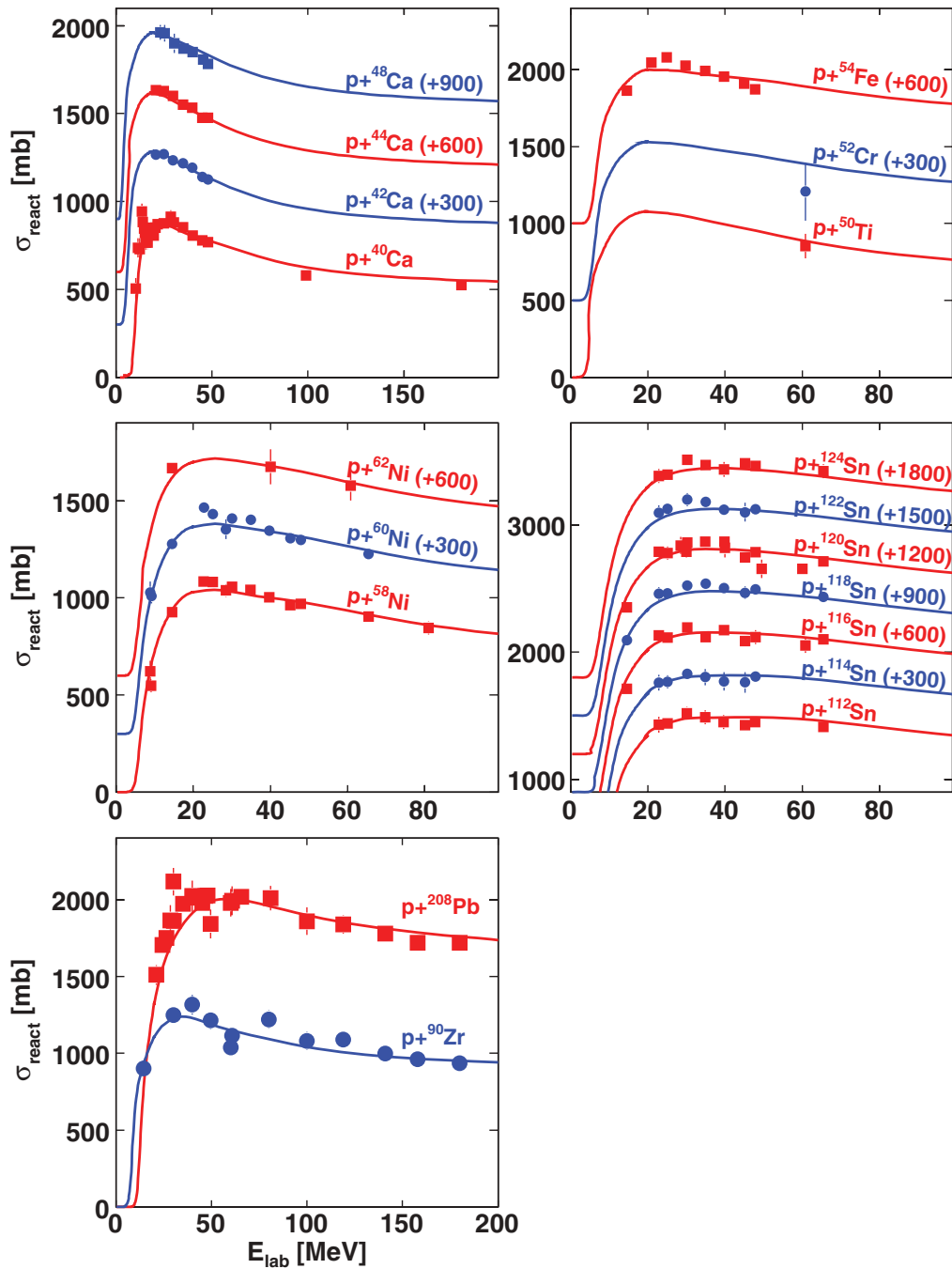
FIG. 8. (Color online) Fits to proton total reaction cross sections. For clarity, data and curves have been progressively shifted up along the vertical axis with increasing energy. The amount of the shift is indicated for each curve.

associated with asymmetry energy. The quantity $\alpha^{\mathrm{vol}}\overline{V_C}$ is the difference in the nuclear potential between a proton and a neutron for a $Z = N$ nucleus and is called the Coulomb correction.

The systematics of the V_0^{HF} values extracted from this work do not need to explicitly use the Coulomb correction as the energy dependence in Eq. (33) is always with respect to the Fermi energy, which includes the Coulomb energy. For example, Mahaux and Sartor [46] noted that the difference

in neutron and proton Fermi energies for ^{40}Ca is $\overline{V_C}$. More generally, the Fermi energies can be parametrized as [47]

$$E_F = E_F{}^0 \pm E_F{}^1 \frac{N - Z}{A} + \overline{V_C}. \tag{45}$$

Figure 22 shows the $E_F - \overline{V_C}$ values from the systems studied in this work and the lines are fits, to the above equation, giving $E_F{}^0 = -13.9$ MeV and $E_F{}^1 = -42.9$ MeV. To first order, we
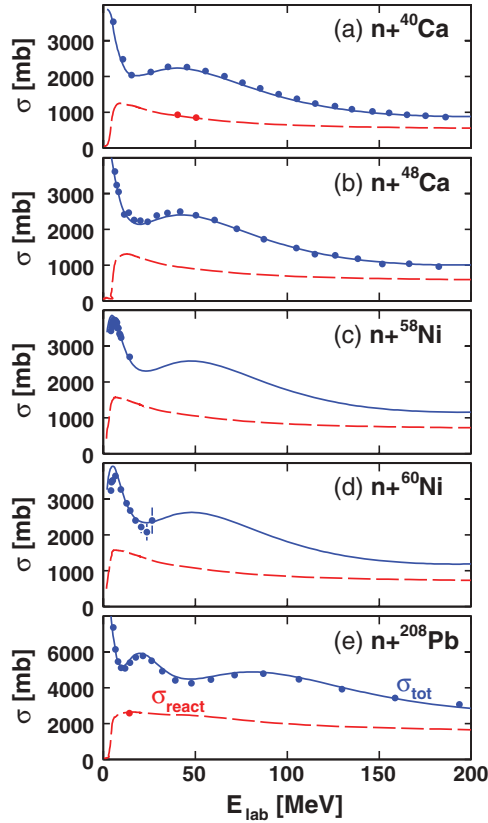
FIG. 9. (Color online) Comparison of experimental (data points) and fitted (curves) total and reaction cross sections for the indicated neutron-induced reactions. The solid and dashed curves are for the total and reaction cross sections, respectively. For clarity, some of the experimental points for the total reaction cross sections have been suppressed.

can rewrite Eq. (33) to include the asymmetry dependence as

$$V_{\text{vol}}^{\text{HF}} = V_{00}^{\text{HF}} \pm V_1^{\text{HF}} \frac{N-Z}{A} - \alpha^{\text{vol}}(E - E_F). \quad (46)$$

Inserting the Fermi energy from Eq. (45) into the above equation yields the standard optical-model potential of Eq. (43) with

$$V_0^{\text{OM}} = V_{00}^{\text{HF}} + \alpha^{\text{vol}} E_F{}^0, \quad (47)$$

$$V_1^{\text{OM}} = V_1^{\text{HF}} + \alpha^{\text{vol}} E_F{}^1. \quad (48)$$

The values of the terms in Eq. (46) can be obtained from systems where both proton and neutrons are analyzed, i.e.,

$$V_{00}^{\text{HF}} = \frac{V_0^{\text{HF}}(p) + V_0^{\text{HF}}(n)}{2}, \quad (49)$$

$$V_1^{\text{HF}} \frac{N-Z}{A} = \frac{V_0^{\text{HF}}(p) - V_0^{\text{HF}}(n)}{2}. \quad (50)$$

Such values are plotted in Figs. 22(b) and 22(c) for the first and second terms, respectively. The linear asymmetry dependence of the second term is readily observed in Fig. 22(c) and the line is a linear fit giving $V_1^{\text{HF}} = 37.7$ MeV. The value of V_{00}^{HF} in Fig. 22(b) is roughly constant for the systems plotted, but there is a small mass dependence, which is fit with the linear
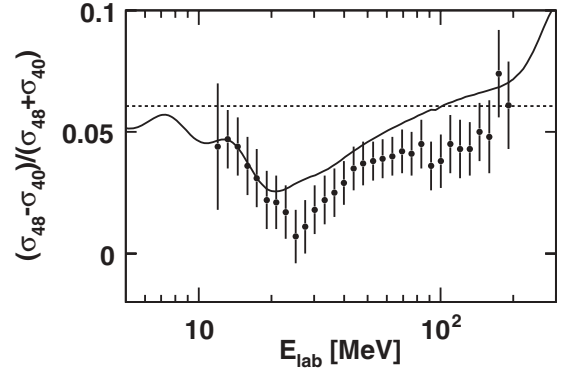
FIG. 10. Ratio of the difference to the sum of the total cross sections of neutrons on ^{48}Ca and ^{40}Ca targets. As a reference, the dashed line shows the magnitude just from the change in radius assuming an $A^{1/3}$ dependence. The curve shows the fit to the experimental data points from Ref. [25].

relationship

$$V_{00}^{\text{HF}} = 60.4 - 0.041A \quad (51)$$

and is shown by the line in the figure. By using all the fitted values and taking an average value of 0.45 for α^{vol} from Table I, we obtain, from Eqs. (47) and (48), $V_0^{\text{OM}} = 54.1 - 0.041A$ MeV and $V_1^{\text{OM}} = 18.4$ MeV, which are close to the values of 52.9 and 13.1 MeV obtained from the global fits of Varner *et al.* [20].

The term V_1^{OM} represents the potential part of the asymmetry energy. When our value for this term is added to the standard value of the asymmetry kinetic energy for saturated nuclear matter of 12 MeV [48] (which is 5/9 of the mean nucleon kinetic energy), a total asymmetry energy of 30–31 MeV is obtained. This value can be compared to those extracted from the Seeger's mass formula [49] or the droplet model [50] with values of 30.6 and 36.8 MeV, respectively. The sum of our potential contribution and the standard kinetic-energy contribution is also in close agreement with the value of 32.4 MeV found by Danielewicz and Lee from the combined
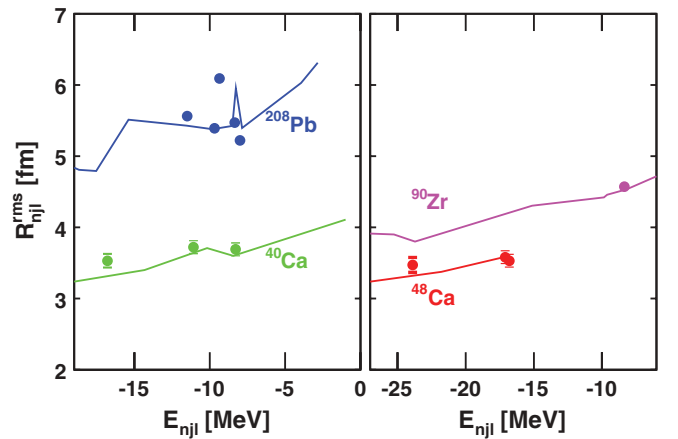
FIG. 11. (Color online) Plot of the rms radii vs energy of the single-particle level $E_{n\ell j}$. The data points are values derived from the $(e, e'p)$ measurements in Table XII and the curves are fits from this work. Note the experimental (fitted) radii are plotted vs the experimental (fitted) $E_{n\ell j}$ values.
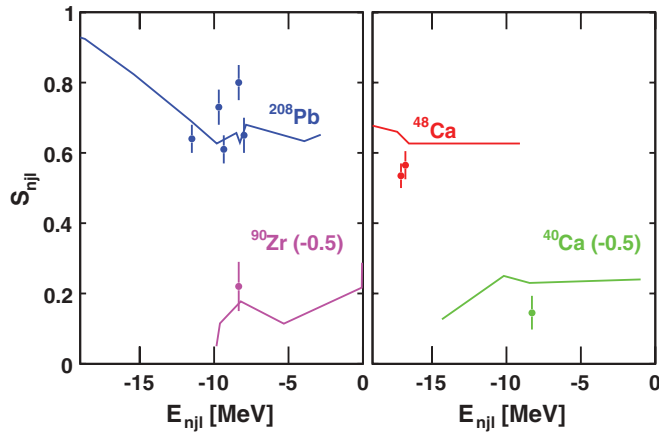
FIG. 12. (Color online) same as in Fig. 11, but for the spectroscopic factors relative to the independent-particle-model values.

FIG. 13. (Color online) Comparison of experimental (data points) and fitted single-particle energies for (a) Ca, (b) Ni, (c) Sn, and (d) ^{92}Mo levels. The dashed curves indicate the Fermi energies.

constraints of a global-mass fit and the mass differences of isobaric analog states [51].

The nonlocality parameter α^{vol} represents the momentum-dependent effective mass of $\widetilde{m}/m$ of 0.49 in the center of the nucleus for the Ca region. It rises to 0.62 for ^{208}Pb. These values do seem to approach the typical values of 0.7 from nuclear-matter calculations [52]. The asymmetry dependence of α^{vol} from the $\alpha_{NZ}^{\mathrm{vol}}$ term in Eq. (34) can be understood as specifying different nonlocalities associated with the V_{00}^{HF} and V_{1}^{HF} components. The isoscalar component (V_{00}^{HF}) has much stronger nonlocality (energy dependence) than than the isovector component (V_{1}^{HF}), which is consistent with that found by Rook [53].

C. Spectroscopic factors

In the independent-particle model, the strength of a single-particle level is located at a single energy. However, the action of the correlations spreads this strength out to higher and lower energies and the energy distribution is described by the spectral function

$$S_{\ell j}(r; E) = \frac{1}{\pi} \mathrm{Im} G_{\ell j}(r, r; E), \qquad (52)$$

and the spectral strength as a function of energy for a given ℓj combination is given by

$$S_{\ell j}(E) = \int_{0}^{\infty} dr \, r^{2} \, S_{\ell j}(r; E). \qquad (53)$$

The propagator $G_{\ell j}$ is the solution of the Dyson equation in coordinate space [15]. For a valence level, the strength function consists of a delta function at the IPM level energy plus continuum contributions at lower and higher energies. The spectroscopic factor represents the integral of the delta-function component and gives the reduction in the localized strength at the IPM level energy due to correlations.

Spectroscopic factors can be estimated from the fitted potentials using Eq. (14). There is more uncertainty in the absolute values of the spectroscopic factors than in the relative values, which are of interest when comparing differences
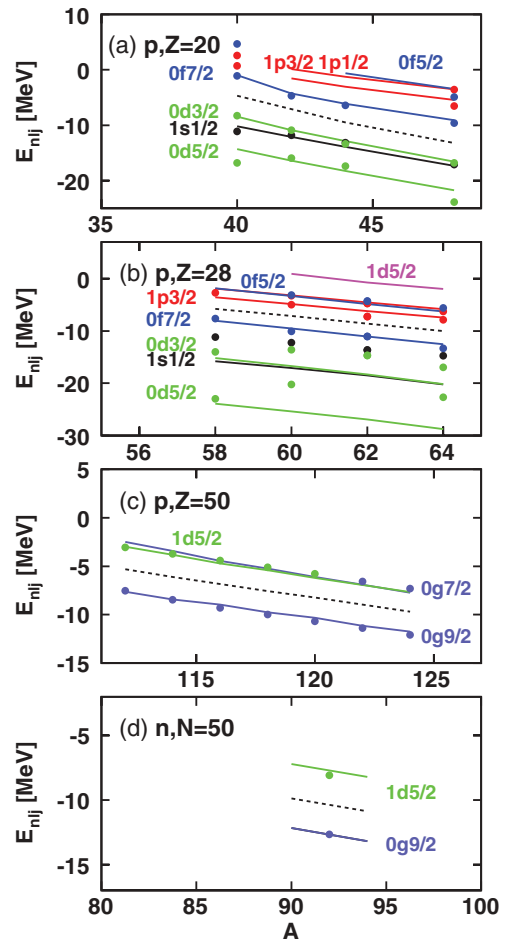
between levels or between nuclei or the asymmetry dependence. For example, the parameter α in Eq. (27) is not well constrained in the fits, and modifications to its value will move all the spectroscopic factors in the same direction, either to larger or smaller values, preserving relative values [9,14]. This factor is closely related to the strength of the repulsive core and the tensor force of the underlying nucleon-nucleon interaction [8]. Data from the $(e, e'p)$ reaction on ^{208}Pb suggest a depletion of the Fermi sea and a corresponding reduction of spectroscopic factors of about 15% or slightly more as being due to the effect of short-range and tensor correlations [54] (see also below).

The asymmetry dependence of the extracted nucleon potentials will induce an asymmetry dependence of the spectroscopic factors in the DOM. However, there are other factors that are also important. Let us concentrate on the Sn isotopes to begin with. The spectroscopic factors deduced from the fitted potential with Eq. (14) for the valence-hole levels are plotted in Fig. 23. The spectroscopic strength of the valence levels is more sensitive to the imaginary surface potential than are the deeper-lying states. The protons show an overall decrease in the spectroscopic strength with increasing A, which is associated with the increase in the imaginary

FIG. 14. (Color online) Comparison of experimental (exp) and fitted (calc) single-particle-level energies for protons in ^{40}Ca and ^{58}Ni. The single experimental $0p$ state in the ^{40}Ca is the average of the $0p_{3/2}$ and $0p_{1/2}$ as the two levels were not resolved. Fermi energies are indicated by the dashed lines.

surface potential. However, the magnitude of the effect is moderate; the 65% change in W_{max}^{sur} from ^{112}Sn to ^{124}Sn corresponds to only a 14% change in the spectroscopic factor. To understand this, we plot in Fig. 24 the radial dependence of the two quantities in Eq. (14) used to calculate this quantity: the reduced wave function and the energy-dependent effect mass. At the peak in the surface, the effective masses from ^{112}Sn and ^{124}Sn differ by 30%, but elsewhere by a smaller amount. [The enhancement above unity at small radii in Fig. 24 is associated with the volume imaginary potential, which has only a very small asymmetry dependence (Sec. IV)]. When averaged over the $0g_{9/2}$ wave function, this difference in effective mass corresponds to the above-mentioned 14% difference.

Beyond the overall decrease, the spectroscopic factor for ^{116}Sn is further lowered as its E_p^{sur} value specifying the gap in the imaginary potential around the Fermi energy [see Eq. (28)] is lower than the values for the neighboring Sn isotopes. This is a consequence of the small Δ_n value for neutrons in this isotope [see Eq. (30)].

The single-particle energies in the fits do not exactly reproduce the experimental values. For the proton $0g_{9/2}$ orbits in these Sn isotopes, the fitted energy is, at most, 390 keV different from these experimental values. To see if this has a significant effect, we have refit all the data so that, instead of adjusting the depth of the Hartree-Fock potential to get the correct Fermi energy, we have now readjusted it to get the correct $0g_{9/2}$ level energy. This refit makes only very small modifications in the values of the fit parameters. The spectroscopic factors from these new fits (open data points) are compared to the older values (filled data points) in Fig. 25. The differences in the two spectroscopic factors are quite modest. The largest difference in S, which occurs for the heavier Sn isotopes, is only 0.04. However, the change in spectroscopic factor from ^{112}Sn to ^{124}Sn has now increased to 23%.

FIG. 15. (Color online) Comparison of experimental and fitted, neutron and proton, single-particle levels for the double-closed-shell nuclei ^{48}Ca, ^{40}Ca, and ^{208}Pb. Fermi energies are indicated by the dashed lines.

In Fig. 25, we also show some extrapolated spectroscopic factors for proton $0g_{9/2}$ levels in ^{102}Sn, ^{106}Sn, ^{130}Sn, and ^{132}Sn. To obtain these, we used a linear extrapolation of the W_{max}^{sur} values in Fig. 17. Although we have expressed reservations concerning such a linear extrapolation, these extrapolations will give indications as to the possible largest variations in the spectroscopic factors across the Sn isotopes. For determining the particle-hole gaps Δ_p and Δ_n in Eq. (30) for the ^{102}Sn and ^{106}Sn nuclei, some of the separation energies have not been measured. In these cases, we obtained these quantities from the mass estimates in Ref. [55]. With the linear extrapolation,

FIG. 16. (Color online) Fitted energy dependences of the magnitudes $W^{\text{sur}}(E)$ and $W_0^{\text{vol}}(E)$ of the imaginary surface and volume potentials for the indicated nuclei. The solid and dashed curves are for protons and neutrons, respectively.

the spectroscopic factors show an overall decrease in S by ~ 0.2 from ^{100}Sn to ^{132}Sn. However, for ^{102}Sn and ^{132}Sn, at or near a closed neutron shell, the Δ_n values are relatively larger and there is a relative shift up in the spectroscopic factors, i.e., decrease in correlations.

Since the magnitude of the imaginary surface potential for neutrons is approximately constant, one might expect that the spectroscopic factors (relative to the independent-particle-model values) would also be constant. However, one sees a big drop in Fig. 23 between ^{120}Sn and ^{124}Sn. In the DOM calculations, this is a consequence of the change in character of the valence levels: a $2s_{1/2}$ level for ^{120}Sn and a $0h_{11/2}$ level for ^{124}Sn. The larger centrifugal potential for the larger ℓ values suppresses the wave function in the center of the nucleus and, thus, enhances it in the surface region (see Fig. 24 comparing the proton $0p_{1/2}$ and $0g_{9/2}$ wave functions). Thus, large ℓ levels, such as the $0h_{11/2}$, couple more strongly to the imaginary surface potential, decreasing the spectroscopic factor. The magnitude of this effect is comparable to that from the asymmetry dependence of the imaginary potentials.

The mass dependence of the proton $0d_{3/2}$ valence-hole spectroscopic factors is displayed in Fig. 26 for Ca isotopes. This can be compared to the data from the $(e, e'p)$ reactions indicated by the data points. As mentioned before,

the values calculated from the DOM are slightly higher. Their mass dependence is again strongly anticorrelated with the imaginary surface potential [see, for example, Fig. 21(a)].

Spectroscopic factors for valence-hole levels derived from knockout reactions exhibit a strong dependence on asymmetry. Gade *et al.* [10,11] have considered reduction factors, i.e., the ratio of the measured spectroscopic factor relative to shell-model predictions. When plotted versus either the separation energy E_{sep}, i.e., the binding energy of the valence level, or ΔE_{sep}, which is $E_{\text{sep}}^p - E_{\text{sep}}^n$ for proton levels and $E_{\text{sep}}^n - E_{\text{sep}}^p$ for neutrons levels, a significant correlation is observed. Both E_{sep} and ΔE_{sep} are related to the neutron-proton asymmetry, and the knockout data imply that the minority species of nucleons experience stronger correlations when the number of the majority species is increased. This is qualitatively consistent with the trend we obtain for protons due to the asymmetry dependence of the imaginary potentials. However, the magnitude of the effect is significantly larger for the data from knockout reactions. The most extreme case is for the $0d_{5/2}$ proton level in ^{32}Ar, where the measured spectroscopic factor from the knockout reactions is $\sim 21\%$ of the IPM value.

The spectroscopic factors obtained in this paper for the $Z = 20$, 28 and $N = 28$ fits are plotted versus E_{sep} and ΔE_{sep} in Figs. 27(a) and 27(b), respectively. We have chosen not to include the heavier systems as the Gade work is confined to lighter masses. Because we studied only stable nuclei, we do not cover as large a range of either E_{sep} or ΔE_{sep} as Gade *et al.* Even so, our results show no significant trends with either E_{sep} and ΔE_{sep}. In fact, the expected trends associated with the asymmetry dependence of the imaginary potential shown in Fig. 18 have been partly obscured by the fluctuations due to the different ℓ values of the various valence levels and by the chosen abscissa coordinates. Our results are consistent with the much weaker ΔE_{sep} trend obtained recently by Lee *et al.* using transfer reactions [12]. Microscopic calculations based on the Faddeev random-phase approximation also do not generate a very pronounced separation-energy dependence when neutron-rich nuclei are considered [18]. This approach may shed some light on the extracted increase of the imaginary part of the surface potential obtained in this paper, since it
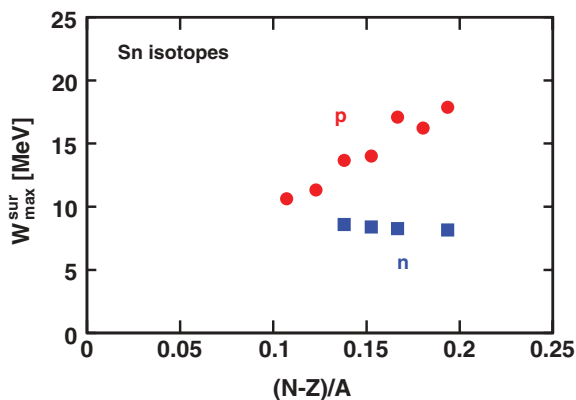
FIG. 17. (Color online) The maximum of the fitted imaginary surface potential obtained for Sn isotopes.
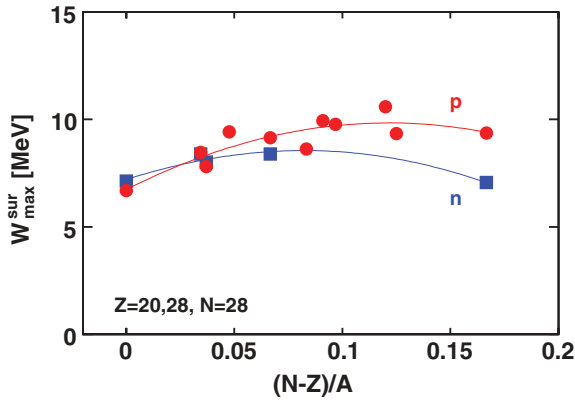
FIG. 18. (Color online) The maximum of the fitted imaginary surface potentials obtained for $Z = 20, 28$ and $N = 28$ are shown as the data points. The curves show smoothed asymmetry dependence through the points.

explicitly calculates the influence of long-range correlations on the nucleon self-energy or optical-model potential. The assumed symmetry around the Fermi energy of the imaginary DOM surface potential can also be investigated using this method.

VI. OCCUPATION PROBABILITIES

The occupation probability characterizes the total strength of a single-particle orbit below the Fermi energy. The discussion of occupation probabilities requires consideration of the recent work reported in Ref. [15]. A nonlocal version of the real HF potential was employed in that work to replace the local but energy-dependent potential of the traditional DOM approach, and the Dyson equation is solved to give the single-particle propagator $G_{\ell j}$ for a given ℓj combination. The advantage of this strategy is that it becomes possible to interpret the DOM potential directly as a nucleon self-energy. The calculation of the propagator below the Fermi energy with the correct normalization is then possible, yielding access to such properties as the (charge) density distribution and
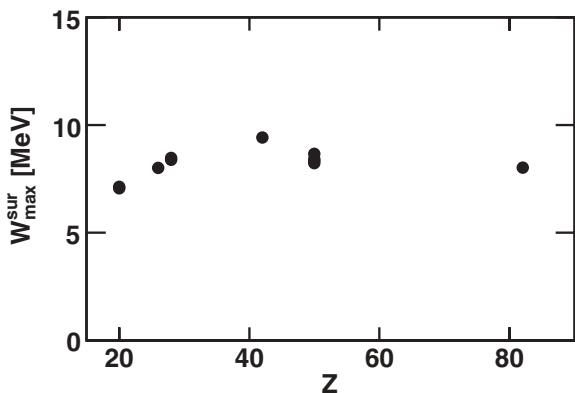
FIG. 19. The maximum of the fitted imaginary surface potential obtained for neutrons for all systems studied plotted as a function of proton number Z.
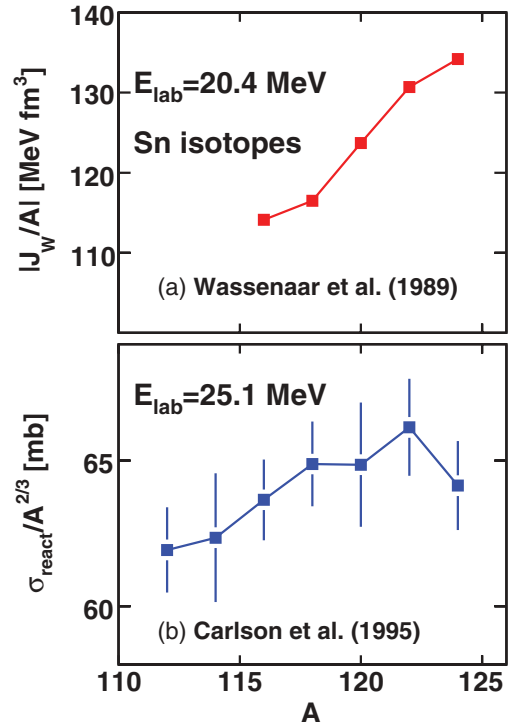
FIG. 20. (Color online) Mass dependence for Sn isotopes of (a) the integrated imaginary potential for protons from the fits to elastic-scattering data obtained by Wassenaar *et al.* scaled by A^{-1} [42] and (b) the proton reaction cross section measured at 25 MeV by Carlson *et al.* [44] scaled by $A^{-2/3}$.

momentum distribution, provided the appropriate correction of the dispersive part of the DOM potential is made [14]. For details, we refer to Ref. [15]. To obtain the occupation numbers of valence orbits, it is necessary to interpret the wave functions in Eq. (13) as overlap functions normalized to 1. Multiplying the one-body density matrix

$$n_{\ell j}(r', r) = \frac{1}{\pi} \int_{-\infty}^{E_F} dE \, \text{Im} G_{\ell j}(r, r'; E)$$
$$= \langle \Psi_0^A | a_{r'\ell j}^\dagger a_{r\ell j} | \Psi_0^A \rangle, \tag{54}$$

with a wave function at r and one at r' and integrating over these variables, yields the occupation number for such an orbit [15]. One observation of this recent work for levels in ^{40}Ca is that the conventional DOM expressions for the occupation numbers given in Eqs. (16) and (17) may not be sufficiently accurate for levels near the Fermi energy. While this statement involves deviations of a few percent in the ^{40}Ca isotope, it is expected to be a more serious problem when the role of the increased surface imaginary part in Sn isotopes on proton occupation numbers is investigated.

We have therefore constructed nonlocal HF potentials for the protons in Sn isotopes, while keeping the dispersive part from the DOM fits fixed, apart from the well-defined nonlocality enhancement [14]. The nonlocality of the potential is of the standard Gaussian form [33] used in Ref. [15] for ^{40}Ca. The nonlocal potentials were required to reproduce the position
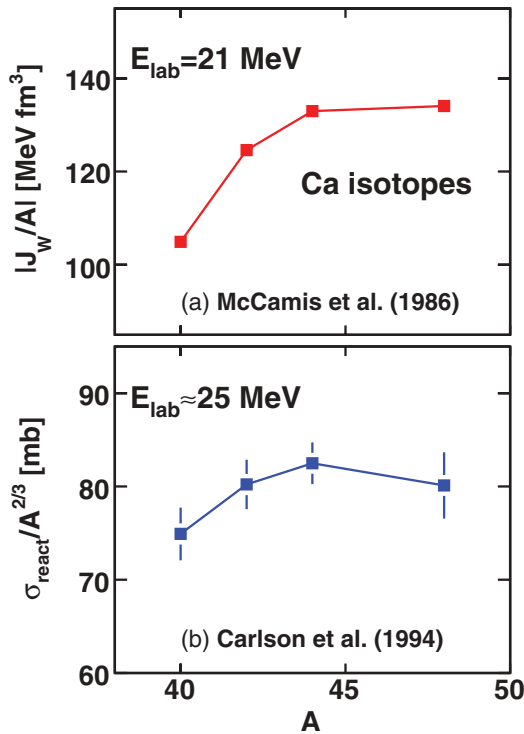
FIG. 21. (Color online) Mass dependence for Ca isotopes of (a) the integrated imaginary potential for protons from the fits to elastic-scattering data obtained by McCamis *et al.* [43] scaled by A^{-1} and (b) the proton reaction cross section measured at $\sim$21 MeV by Carlson *et al.* [45] scaled by $A^{-2/3}$.

of the $0g_{9/2}$ proton level and, where known, to reproduce the mean-square radius of the charge distribution [58]. It is well known that HF calculations only succeed in reproducing the trend of the mean-square radius of the charge distribution for Sn isotopes when an $A^{1/6}$ instead of a conventional $A^{1/3}$ radius dependence is employed [59]. By employing this dependence for the nonlocal HF potential, we are able to reproduce the mean-square charge radius for ^{112}Sn and ^{124}Sn. It was then only necessary to adjust the depth of the potential for each isotope in order to generate the required fit to the position of the $g_{9/2}$ levels and the charge radii. The resulting depths exhibit an essentially linear $N - Z$ dependence.

In Fig. 28, the strength function [Eq. (53)] of the $g_{9/2}$ orbit is shown for a relevant selection of Sn isotopes. Again, the linear extrapolation of $W_{\max}^{\text{sur}}$ is used for ^{102}Sn, ^{106}Sn, ^{130}Sn, and ^{132}Sn. For these valence levels, the strength function consists of a delta function at the IPM level energy plus continuum contributions at higher and lower energies. Only the negative continuum contribution is shown in the figure.

The locations of the delta functions are indicated by the vertical lines, and the height gives the spectroscopic factor (the integral of delta function). The curves represent the continuum and are labeled with the corresponding mass number. These curves representing the strength in the continuum below the Fermi energy clearly reflect the increase in the surface absorption derived from the proton elastic-scattering data
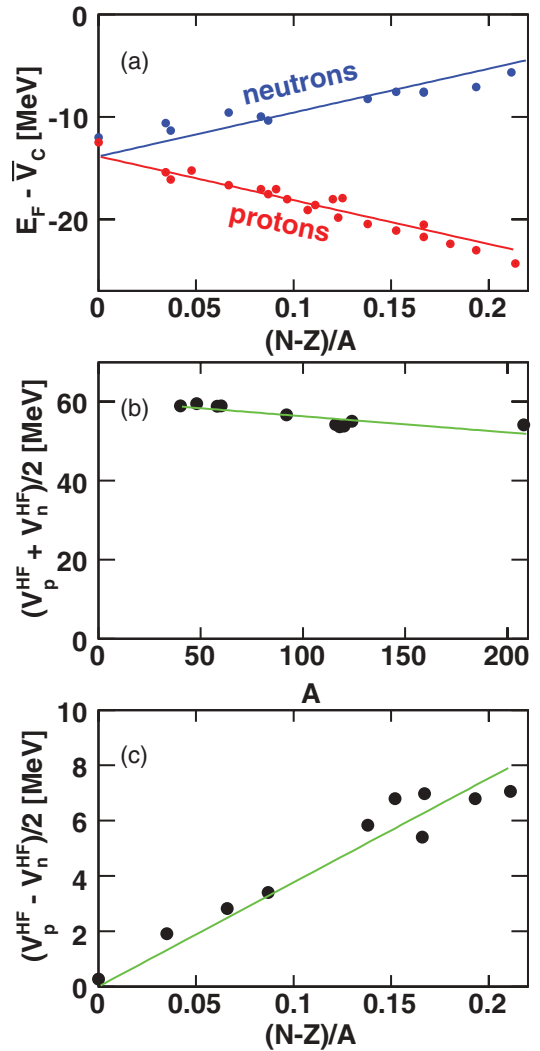
FIG. 22. (Color online) (a) Asymmetry dependence of the Fermi energy corrected for the average Coulomb energy inside the nucleus $\overline{V_C}$. (b) and (c) are derived from the sum and difference of the magnitudes of the Hartree-Fock potentials extracted for protons and neutrons. In all cases, the lines are linear fits (see text).

under the standard DOM assumption that surface imaginary potentials exhibit similar behavior above and below the Fermi energy [14]. In the energy domain below the Fermi energy corresponding to the imaginary surface potential, a distinct increase in the strength can be observed with increasing neutron number. Accompanying this increased strength is a reduction of the corresponding $0g_{9/2}$ spectroscopic factor (triangles in Fig. 28). Quantitative results are reported in Table III for the spectroscopic factors (S_{nl}), strength in the continuum (n_{nl}^c), total occupation number (n_{nl}), where nl refers to the nonlocal version of the DOM for this series of isotopes. In addition, the occupation number (n_l) and spectroscopic factor (S_l) from Eqs. (14), (16), and (17) are listed for the local DOM using parameters from the refits where the $0g_{9/2}$ level energies are exactly reproduced. The increase in the continuum contribution of the occupation number ends with ^{130}Sn on account of the larger gap between particle and hole states
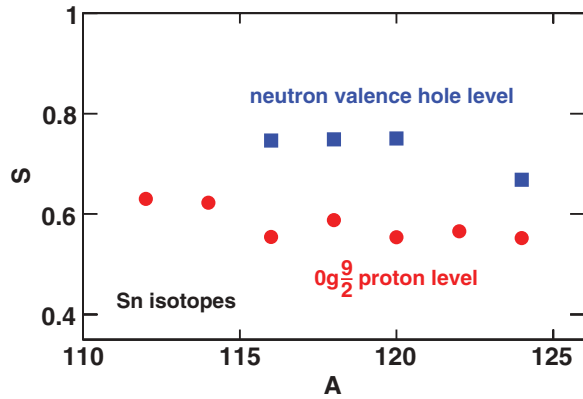
FIG. 23. (Color online) Mass dependence of spectroscopic factors (relative to IPM values) for valence-hole levels deduced from the fitted potentials for Sn isotopes.

for the double-closed-shell nucleus ^{132}Sn, as discussed earlier. We note that the reduction of the $g_{9/2}$ spectroscopic factor with increasing neutron number is accompanied by a weaker reduction of the occupation number. This feature is consistent with the notion that increased surface absorption leads to removal of strength to both sides of the Fermi energy so that the reduction in the occupation should be less (and approximately half of the reduction of the spectroscopic factor for each isotope for a level very near the Fermi energy). While the spectroscopic factors for the $0g_{9/2}$ level in the local DOM are consistent with the nonlocal results, there is a clear disagreement between the occupation numbers obtained by the different versions. This confirms the conclusion of Ref. [15] that occupation numbers obtained from the approximate expressions in Eqs. (16) and (17) may not always be accurate. This is particularly true for a nominally empty level such as the $g_{7/2}$, where the nonlocal version generated an occupation number of 0.15 in ^{130}Sn, whereas the local result is 0.33.
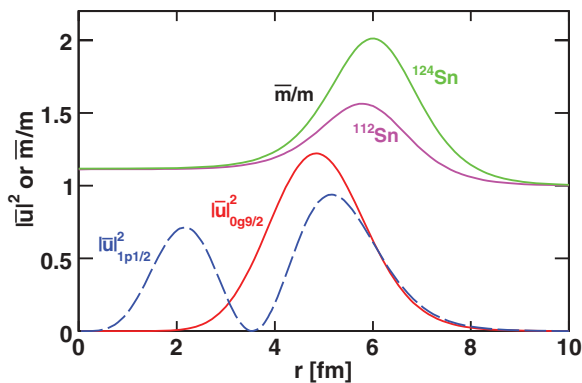
FIG. 24. (Color online) Radial dependence of the energy-dependent effective mass and the square of the reduced wave function. Effective masses are shown for ^{112}Sn and ^{124}Sn and wave functions are shown for the $0g_{9/2}$ and $1p_{1/2}$ proton levels in ^{112}Sn.
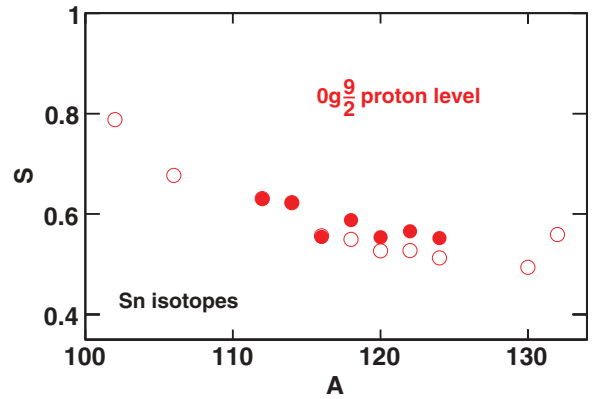
FIG. 25. (Color online) Comparison of proton $0g_{9/2}$ spectroscopic factors (relative to IPM values) for Sn isotopes obtained with the standard fits (filled data points), where the depth of the Hartree-Fock potential was adjusted to reproduce the Fermi energy, to those where the depth was adjusted to reduce the correct $0g_{9/2}$ level energy (open data points). Predictions are also shown for ^{102}Sn, ^{106}Sn, ^{130}Sn, and ^{132}Sn using a linear extrapolation of W_{max}^{sur}.

The $N - Z$ behavior of the proton correlations obtained for Sn isotopes invites consideration of possible future experiments to confirm the trend predicted in Table III. A consistent analysis of the $(d, {}^3\text{He})$ reaction employing a finite-range DWBA approach as in Ref. [57] might be able to shed light on the behavior of the proton $g_{9/2}$ spectroscopic factors by employing light and heavy radioactive Sn isotopes in inverse kinematics. A serious difficulty will be the construction of appropriate optical potentials for these exotic reactions. An alternative experimental approach might be to employ the (d, n) reaction in inverse kinematics for these exotic isotopes and study the behavior of the $g_{7/2}$ spectroscopic factor for the addition of a proton. The spectroscopic factor for this particle level tracks the one for the $g_{9/2}$ hole level reported in Table III to within a few percent.
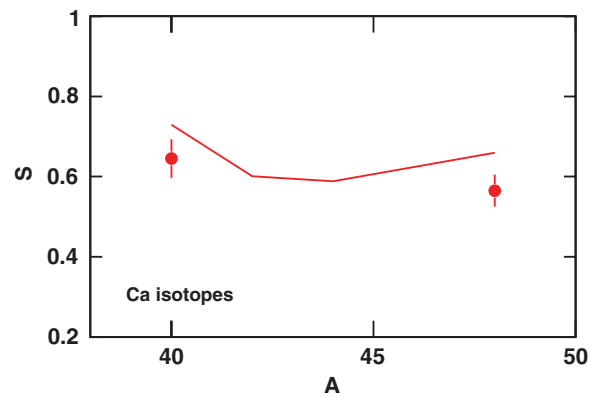
FIG. 26. (Color online) The line connects the calculated mass dependence for spectroscopic factors (relative to IPM values) for proton $0d_{3/2}$ valence-hole levels deduced from the fitted potentials for Ca isotopes. The data points are results from $(e, e'p)$ measurements [56,57].
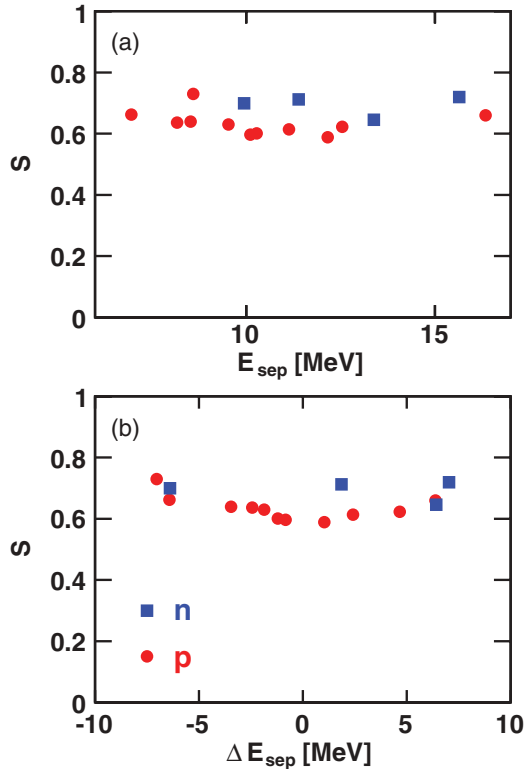
FIG. 27. (Color online) Spectroscopic factors (relative to the independent-particle-model value) for valence-hole levels determined from the fitted potentials. Results are shown for the $Z = 20$, 28 and $N = 28$ and the square and circular points represent neutrons and protons, respectively. In (a), these are plotted versus the separation energy of the level, while in (b), they are plotted versus the difference in proton and neutron separation energies.

We note that the predicted behavior of the proton $g_{9/2}$ spectroscopic factor as a function of $N - Z$ is still mild compared to the deduced behavior of the removal strength using heavy-ion knockout reactions [10,11] in sd-shell nuclei. The spectroscopic factors implied by these experiments are much smaller (or larger) far off stability than generated here for protons in Sn isotopes. An unambiguous test of such small (or large) spectroscopic factors could be provided by performing the corresponding elastic-scattering experiments, at least for protons, in inverse kinematics. Indeed, since the

TABLE III. Spectroscopic factors S (relative to the IPM predictions) and occupation numbers n for the $0g_{9/2}$ proton orbit in Sn isotopes using the nonlocal (nl) and local (l) versions of the DOM.

Isotope	S_{nl}	n_{nl}^c	n_{nl}	n_l	S_l
102	0.80	0.11	0.91	0.86	0.79
106	0.68	0.17	0.85	0.81	0.68
112	0.63	0.20	0.83	0.74	0.63
124	0.50	0.28	0.78	0.62	0.51
130	0.48	0.30	0.78	0.60	0.49
132	0.56	0.25	0.81	0.65	0.56
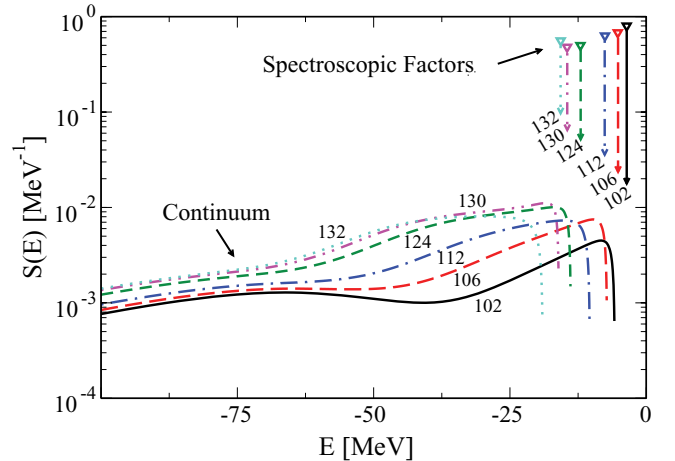
FIG. 28. (Color online) Strength functions of the $g_{9/2}$ proton orbit in different Sn isotopes obtained with the nonlocal calculations. The curves represent the continuum contribution of the strength function and are labeled by the appropriate mass number. Also indicated is the location of the $0g_{9/2}$ quasihole level in the different isotopes. The height of the corresponding vertical lines identifies the spectroscopic factor for each isotope.

implied physics is associated with surface phenomena [60], one would expect that the remaining sp strength occurs in the domain where surface absorption takes place.

As for the spectroscopic factors, it should be kept in mind that relative occupancies are better defined than the absolute values. In Fig. 29, we compare the occupancies for proton levels in ^{208}Pb found in the present work (lines) using Eqs. (16) and (17), with those from van Batenburg [54] (data points). The latter results were derived from $(e, e'p)$ data by assuming a reasonable static Woods-Saxon potential well and spectral shape for each occupied proton level exhibiting an increased width with increasing distance from the Fermi energy. The remaining unknowns are the integrals over these spectral distribution, in other words, the corresponding occupation numbers. The latter are fitted to the data and this procedure generates the data points of Fig. 29 while capable of accurately describing the $(e, e'p)$ cross sections for all mean-field momenta (<270 MeV/c) and binding energies including the lowest $s_{1/2}$ level. We note that the single-particle levels used in Ref. [54] have slightly different energies than the solutions of the fitted DOM potential, which is reflected in Fig. 29. For the deep hole states, our occupancies are slightly larger; however, the relative dependence on the single-particle energy is quite similar. We note again that Eq. (16) is an approximate result, as explained earlier in this section, but we find the agreement with the numbers extracted from experiment encouraging nevertheless.

VII. CONCLUSIONS

The neutron-proton asymmetry dependence of correlations in nuclei has been studied via a dispersive-optical-model analysis giving information on the neutron and proton
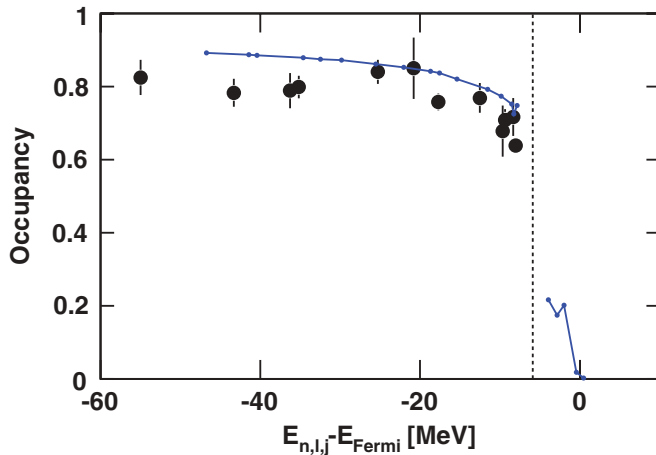
FIG. 29. (Color online) Comparison of proton occupation probabilities in ^{208}Pb. The data points are from van Batenburg [54] and the lines are from this work.

self-energies or optical-model potentials. Elastic-scattering data for a wide range of masses were obtained from previously published studies and, in addition, the neutron elastic-scattering differential cross sections on ^{48}Ca were measured at incident energies of 11.9 and 16.9 MeV. These data were supplemented with published measurements of reaction and total cross sections, the energies of single-particle levels, and some $(e, e'p)$ measurements of rms radii and spectroscopic factors of valence-hole states.

In the dispersive optical model, long- and short-range correlations are described by surface and volume imaginary potentials (self-energies), respectively. From a comparison of proton and neutron data on ^{208}Pb, a small asymmetry dependence of the imaginary volume potential was deduced. The imaginary volume potential was 10% higher for protons. The surface imaginary component showed quite different asymmetry dependences between protons and neutrons. The magnitude of neutron imaginary surface potential was almost independent of mass and asymmetry. The extracted values were within 24% of each other from $A = 40$ to 208. Protons displayed much stronger dependence, although a universal behavior was not found. Stable Sn isotopes displayed a large increase (65%) in the imaginary surface potential with increasing neutron number. The lighter $Z = 20, 28$ and $N = 28$ closed-shell nuclei showed an initial increase, but subsequent saturation with increasing neutron number. These results are only for $N \geqslant Z$ and for nuclei close to stability. For $N < Z$, one would expect from isospin symmetry that the roles of the protons and neutrons would be reversed, i.e., the neutron surface imaginary potential would have an important asymmetry dependence, whereas for protons, there would be little asymmetry dependence.

The large observed asymmetry dependence for protons gives rise to only a modest asymmetry dependence of spectroscopic factors. The differences in spectroscopic

factors produced by this effect are of a similar magnitude to that between levels with high- and low-ℓ values. The asymmetry dependence of spectroscopic factors predicted by the dispersive-optical-model analysis is consistent with recent transfer-reaction measurements [12], but significantly smaller than that suggested by knock-out reactions [10,11]. However, we caution that our results are only for stable nuclei and additional physics may be relevant for the more exotic nuclei probed with the knockout reactions, possibly related to the encroaching continuum [61]. However, we note that extrapolating the present DOM framework to more exotic nuclei will provide a benchmark for gauging the magnitude of any additional physics.

The dispersive-optical-model calculations are local. The effect of nonlocality was examined by replacing the energy-dependent real potential by a energy-independent nonlocal version and solving the Dyson equation for the single-particle propagator. For levels near the Fermi energy, the resulting spectroscopic factors are consistent with the values obtained using the fitted local potential and Mahaux's approximations. However, for the occupation probabilities in Sn isotopes, this is not the case. Nonlocal calculations are necessary for these quantities.

APPENDIX: DATA REFERENCES

The elastic-scattering data sets for both protons and neutrons used in the fitting are listed in Tables IV to X along with the appropriate references. Data sets with energies up to 200 MeV were included, and only nuclei for which there are measurements near 20 MeV, where the imaginary surface potential peaks, were considered. For the $Z = 20, 28$ and $N = 28$ systems, there are 200 sets of elastic-scattering differential cross sections and 17 sets of analyzing power measurements. For the $N = 50$, Sn, and ^{208}Pb systems, we found 37, 55, and 49 data sets of differential cross sections and 15, 22, and 22 data sets of analyzing power measurements, respectively.

Single-particle energies $E_{n\ell j}$ were obtained from Refs. [62–68]. For the Sn isotopes and $N = 50$ nuclei, where no extensive list of single-particle energies could be found, we only fitted the first valence particle and last hole levels $\{E_F^+$ and E_F^- [Eqs. (7) and (8)]\}.

Reaction and total cross-section data used are listed in Table XI and $(e, e'p)$ extractions of spectroscopic factors and rms radii are listed in Table XII.

TABLE IV. Elastic-scattering data for p + Ca reactions used in the fits.

E (MeV)	$\frac{d\sigma}{d\Omega}$	A_y	Reference
	$p+^{40}$Ca		
17.57	x		[69]
19.57	x		[39]
21.0	x	x	[43,70]
25.0	x		[43]
26.3	x	x	[43,71]
30.0	x		[43]
30.3		x	[72]
35.0	x		[43]
40.0	x	x	[43,73]
45.0	x		[43]
48.0	x		[43]
49.0		x	[74]
61.4	x		[75]
65.0	x	x	[76]
80.2	x	x	[34,77]
100.6	x	x	[78]
135.1	x		[34]
152.0	x	x	[79]
160.0	x	x	[34,77]
181.0	x	x	[34,77]
200.0	x	x	[80]
	$p+^{42}$Ca		
9.0	x		[81]
12.0	x		[81]
21.0	x		[43]
25.0	x		[43]
30.0	x		[43]
35.0	x		[43]
40.0	x		[43]
45.0	x		[43]
48.4	x		[43]
65.0	x	x	[76]
	$p+^{44}$Ca		
9.0	x		[81]
10.75	x		[82]
12.0	x		[81]
14.15	x		[82]
15.61	x		[82]
21.0	x		[43]
25.0	x		[43]
30.0	x		[43]
40.0	x		[43]
45.0	x		[43]
48.4	x		[43]
65.0	x	x	[76]
	$p+^{48}$Ca		
8.0	x	x	[83]
10.0	x	x	[83]
12.0	x	x	[83]
14.03	x	x	[82]
15.05	x	x	[82]
15.65	x	x	[82]
21.0	x		[43]
25.0	x		[43]
30.0	x		[43]
35.0	x		[43]
40.0	x		[43]
45.0	x		[43]
48.4	x		[43]
65.0	x	x	[76]
200.0	x	x	[80]

TABLE V. Elastic-scattering data for n + Ca and p + N = 20 isotone reactions used in the fits.

E (MeV)	$\frac{d\sigma}{d\Omega}$	A_y	Reference
	$n+^{40}$Ca		
9.9	x	x	[29]
11.0	x		[84]
11.9	x	x	[29]
13.9	x	x	[29,30]
16.9	x	x	[30]
19.0	x		[85]
20.0	x		[84]
21.7	x		[85]
25.5	x		[85]
26.0	x		[84]
30.0	x		[86]
40.0	x		[86]
65.0	x		[87]
75.0	x		[87]
85.0	x		[87]
95.0	x		[87]
107.5	x		[87]
127.5	x		[87]
155.0	x		[87]
185.0	x		[87]
	$n+^{48}$Ca		
7.97	x		[88]
11.9	x	x	This work
16.9	x	x	This work
	$p+^{50}$Ti		
6.0	x		[89]
11.0	x	x	[90]
14.15	x	x	[82,91]
15.35	x	x	[82,91]
16.0	x	x	[20,92]
18.0	x	x	[90]
18.6	x	x	[93]
18.6		x	[94]
39.9	x		[95]
65.0	x	x	[96]
	$p+^{52}$Cr		
10.77	x	x	[82,91]
14.0		x	[97]
15.35	x	x	[82,91]
16.5		x	[93]
17.5	x		[98]
18.6	x	x	[93]
39.9	x		[95]
	$p+^{54}$Fe		
9.69	x	x	[99]
12.0	x		[100]
16.0	x	x	[20,92]
17.2	x	x	[101]
18.6	x		[93]
19.6	x		[102]
20.4	x	x	[101]
24.6	x		[101]
30.4	x	x	[103]
35.2	x		[104,105]
39.8	x		[106]
65.0	x	x	[96]

TABLE VI. Elastic-scattering data for $n+^{54}$Fe and $p+^{58}$Ni reactions used in the fits.

E (MeV)	$\frac{d\sigma}{d\Omega}$	A_y	Reference
	$n+^{54}$Fe		
5.5	x		[107]
7.0	x		[107]
7.96	x		[26]
8.5	x		[107]
9.94	x	x	[107]
11.0	x		[108]
11.93	x		[26]
13.9	x	x	[26,109,110]
14.7	x		[111]
16.9	x	x	[110]
20.0	x		[108]
22.0	x		[108]
24.0	x		[108]
26.0	x		[108]
	$p+^{58}$Ni		
7.0	x		[100]
8.0	x		[100]
9.0	x		[100]
9.51	x	x	[99]
10.0	x		[100]
11.0	x		[100]
12.0	x		[100]
14.0	x		[97]
16.0	x	x	[20,92]
18.6	x	x	[93]
21.0	x	x	[112]
22.2	x		[113]
24.6	x		[101]
26.3	x		[71]
29.0	x		[114]
30.3	x		[115]
35.2	x		[104,105]
40.0	x		[73,116]
49.0		x	[114]
60.2		x	[117]
61.4		x	[75]
65.0	x	x	[96]
100.0	x		[118]
160.0	x		[119]
172.0	x		[120]
178.0	x	x	[121]
192.0	x	x	[122]

TABLE VII. Elastic-scattering data for $p+^{60,62,64}$Ni and $n+^{58}$Ni reactions used in the fits.

E (MeV)	$\frac{d\sigma}{d\Omega}$	A_y	Reference
	$p+^{60}$Ni		
7.0	x		[100]
8.0	x		[100]
9.0	x		[100]
10.0	x		[100]
11.0	x		[100,123]
12.0	x		[100]
14.0	x		[97]
14.4	x	x	[124]
15.4	x	x	[124]
16.0	x	x	[20,92]
17.8		x	[125]
18.6	x	x	[93]
20.4	x	x	[42]
24.6	x		[101]
29.0	x		[114]
30.0	x		[71]
30.3	x		[115]
40.0	x		[116]
49.0		x	[114]
55.0	x		[126]
65.0	x	x	[96]
178.0	x	x	[121]
	$p+^{62}$Ni		
8.02	x		[127]
11.0	x	x	[123]
12.0	x		[100]
14.0		x	[97]
16.0	x		[128]
16.5		x	[93]
18.6	x	x	[93]
20.4	x	x	[101]
24.6	x		[101]
39.6	x	x	[129]
65.0	x	x	[96]
156.0	x		[130]
	$p+^{64}$Ni		
9.69	x	x	[99]
11.0	x		[123]
12.0	x		[100]
16.0	x		[128]
20.4	x	x	[42]
39.6	x	x	[129]
65.0	x	x	[96]
	$n+^{58}$Ni		
4.5	x		[131]
5.5	x		[131]
6.5	x		[131]
7.5	x		[131]
8.4	x		[131]
9.92		x	[132]
9.99	x		[131]
11.952	x		[132]
13.91		x	[132]
14.0	x		[131]
16.934	x	x	[110]
21.5	x		[131]
24.0	x		[133]

TABLE VIII. Elastic-scattering data for $n+{}^{60}$Ni reactions and reactions with $N=50$ isotones used in the fits.

E (MeV)	$\frac{d\sigma}{d\Omega}$	A_y	Reference
	$n+{}^{60}$Ni		
5.0	x		[134]
6.0	x		[134]
7.0	x		[134]
7.904	x		[132]
9.943		x	[110]
9.958	x	x	[132]
11.952	x		[132]
13.91		x	[132]
14.7	x		[111]
24.0	x		[133]
	$p+{}^{90}$Zr		
5.57	x		[135]
6.57	x		[135]
7.97	x		[135]
8.6	x		[135]
9.6	x	x	[99]
12.7	x		[136]
14.7	x		[137]
16.0	x	x	[92]
18.8	x		[138]
20.25		x	[139]
22.5	x		[140]
25.05	x		[141]
30.0	x	x	[142]
40.0	x		[143]
40.0	x	x	[73]
49.4	x	x	[144]
61.4	x		[75]
65.0	x	x	[96]
79.6		x	[77]
80.0	x		[34]
98.7		x	[77]
100.0	x		[118]
134.8		x	[77]
135.0	x		[34]
160.0	x	x	[34,77]
185.0		x	[145]
	$p+{}^{92}$Mo		
12.5	x		[146]
15.0	x		[147]
19.8	x		[148]
20.25		x	[139]
22.27	x		[149]
30.0	x	x	[142]
30.3	x	x	[148]
49.45	x		[148]
	$n+{}^{92}$Mo		
7.0	x		[150]
9.0	x		[150]
11.0	x		[150]
20.0	x		[150]
26.0	x		[150]

TABLE IX. Elastic-scattering data for Sn reactions used in the fits.

E (MeV)	$\frac{d\sigma}{d\Omega}$	A_y	Reference
	$p+{}^{112}$Sn		
16.0	x		[151]
30.4	x		[152]
	$p+{}^{114}$Sn		
30.4	x		[152]
	$p+{}^{116}$Sn		
16.0	x	x	[153]
21.0	x	x	[112]
30.4	x	x	[152]
39.6	x		[154]
61.4	x		[75]
	$p+{}^{118}$Sn		
16.0	x		[151]
20.4	x	x	[42]
30.4	x		[152]
39.6	x	x	[154]
49.35	x		[144]
	$p+{}^{120}$Sn		
9.8	x	x	[99]
16.0	x	x	[153]
20.4	x	x	[42]
24.6	x	x	[42]
30.0	x	x	[155,156]
39.6	x	x	[154]
49.35	x		[144]
100.0	x	x	[77,118]
104.0	x	x	[157]
156.0	x		[130]
	$p+{}^{122}$Sn		
16.0	x		[151]
20.4	x	x	[42]
30.4	x		[152]
39.6	x	x	[154]
49.35	x		[144]
	$p+{}^{124}$Sn		
16.0	x	x	[153]
20.4	x	x	[42]
30.4	x		[152]
39.6	x	x	[154]
49.35	x		[144]
	$n+{}^{116}$Sn		
9.95	x	x	[132]
11.0	x		[158]
13.94	x	x	[132]
24.0	x		[158]
	$n+{}^{118}$Sn		
11.0	x		[158]
24.0	x		[158]
	$n+{}^{120}$Sn		
9.94	x	x	[132]
11.0	x		[158]
13.92	x	x	[132]
16.91	x		[132]
	$n+{}^{124}$Sn		
11.0	x		[158]
24.0	x		[158]

TABLE X. Elastic-scattering data for reactions on ^{208}Pb used in the fits.

E (MeV)	$\frac{d\sigma}{d\Omega}$	A_y	Reference
	$p+^{208}$Pb		
9.0		x	[159]
11.0	x		[160]
12.98	x	x	[161]
16.0	x	x	[20,92]
21.0	x		[162]
24.1	x		[162]
26.3	x	x	[71,162]
29.1		x	[114]
30.3	x	x	[162,163]
35.0	x		[162]
40.0	x	x	[73]
45.0	x		[162]
47.3	x		[162]
49.3	x	x	[144]
61.0	x		[75]
65.0	x	x	[96]
79.8		x	[77]
80.0	x		[34]
98.0		x	[77]
101.4	x		[118]
121.0	x		[34]
155.0	x	x	[164]
160.0	x	x	[34,77]
182.0	x	x	[34,77]
185.0	x	x	[162]
200.0	x	x	[165]
	$n+^{208}$Pb		
4.0	x		[166]
5.0	x		[166]
5.97		x	[167]
6.0	x		[166]
6.97		x	[167]
7.0	x		[166]
7.97	x	x	[167]
8.5	x		[107]
8.96		x	[167]
9.0	x		[168]
9.97	x	x	[169]
11.0	x		[168]
13.9	x	x	[170]
14.6	x		[171]
16.9	x		[172]
20.0	x		[173]
22.0	x		[173]
24.0	x		[173]
26.0	x		[168]
30.3	x		[174]
40.0	x		[174]
65.0	x		[87]
75.0	x		[87]
85.0	x		[87]
95.0	x		[87]
96.0	x		[175]
107.5	x		[87]
127.5	x		[87]
155.0	x		[87]
185.0	x		[87]

TABLE XI. References for total and reaction cross sections used in this paper.

Reaction	Reference	Reaction	Reference
$p+^{40}$Ca	[176–178]	$n+^{60}$Ni	[179–182]
$n+^{40}$Ca	[25,183–187]	$p+^{62}$Ni	[188,189]
$p+^{42}$Ca	[45]	$p+^{64}$Ni	[188,189]
$p+^{44}$Ca	[45]	$p+^{90}$Zr	[188–191]
$p+^{44}$Ca	[192]	$p+^{112}$Sn	[44,193]
$p+^{48}$Ca	[45]	$p+^{114}$Sn	[44]
$n+^{48}$Ca	[25]	$p+^{116}$Sn	[44,188,189,193]
$p+^{50}$Ti	[189]	$p+^{118}$Sn	[44,188,193]
$p+^{52}$Cr	[189]	$p+^{120}$Sn	[44,188,189,193]
$p+^{54}$Fe	[43,188]	$p+^{122}$Sn	[44]
$p+^{58}$Ni	[178,188,191,193–195]	$p+^{124}$Sn	[44,193]
$n+^{58}$Ni	[131,179,180]	$p+^{208}$Pb	[177,178,189]
$p+^{60}$Ni	[178,188,193–195]	$n+^{208}$Pb	[196,197]

TABLE XII. Spectroscopic factors (relative to the independent-particle-model value) $S_{n\ell j}$ and rms radii $R_{n\ell j}^{\text{rms}}$ extracted for the listed single-particle levels from referenced $(e, e'p)$ data that were used in the fits.

Nucleus	s.p. level	$S_{n\ell j}$	$R_{n\ell j}^{\text{rms}}$ (fm)	Reference
^{40}Ca	$0d_{5/2}$		3.53 ± 0.11	[56,57]
	$1s_{1/2}$		3.72 ± 0.10	
	$0d_{3/2}$	0.645 ± 0.048	3.69 ± 0.10	
^{48}Ca	$0d_{5/2}$		3.47 ± 0.13	[56,57]
	$0d_{3/2}$	0.565 ± 0.040	3.53 ± 0.10	
	$1s_{1/2}$	0.535 ± 0.035	3.58 ± 0.10	
^{90}Zr	$1p_{1/2}$	0.72 ± 0.07	4.57 ± 0.02	[198]
^{208}Pb	$2s_{1/2}$	0.65 ± 0.05	5.22 ± 0.05	[199,200]
	$1d_{3/2}$	0.80 ± 0.05	5.47 ± 0.04	
	$0h_{11/2}$	0.61 ± 0.04	6.09 ± 0.03	
	$1d_{5/2}$	0.73 ± 0.05	5.39 ± 0.03	
	$0g_{7/2}$	0.64 ± 0.04	5.56 ± 0.05	

[1] L. Lapikás, Nucl. Phys. A **553**, 297c (1993).

[2] E. Piasetzky, M. Sargsian, L. Frankfurt, M. Strikman, and J. W. Watson, Phys. Rev. Lett. **97**, 162504 (2006).

[3] K. S. Egiyan *et al.*, Phys. Rev. Lett. **96**, 082501 (2006).

[4] R. Subedi *et al.*, Science **320**, 1476 (2008).

[5] D. Rohe *et al.*, Phys. Rev. Lett. **93**, 182501 (2004).

[6] W. H. Dickhoff and C. Barbieri, Prog. Part. Nucl. Phys. **52**, 377 (2004).

[7] T. Frick, H. Müther, A. Rios, A. Polls, and A. Ramos, Phys. Rev. C **71**, 014313 (2005).

[8] A. Rios, A. Polls, and W. H. Dickhoff, Phys. Rev. C **79**, 064308 (2009).

[9] R. J. Charity, J. M. Mueller, L. G. Sobotka, and W. H. Dickhoff, Phys. Rev. C **76**, 044314 (2007).

[10] A. Gade *et al.*, Phys. Rev. Lett. **93**, 042501 (2004).

[11] A. Gade *et al.*, Phys. Rev. C **77**, 044306 (2008).

[12] J. Lee *et al.*, Phys. Rev. Lett. **104**, 112701 (2010).

[13] W. H. Dickhoff and D. Van Neck, *Many-Body Theory Exposed!*, 2nd ed. (World Scientific, New Jersey, 2008).

[14] C. Mahaux and R. Sartor, Adv. Nucl. Phys. **20**, 1 (1991).

[15] W. H. Dickhoff, D. Van Neck, S. J. Waldecker, R. J. Charity, and L. G. Sobotka, Phys. Rev. C **82**, 054306 (2010).

[16] R. C. Johnson, AIP Conf. Proc. **791**, 128 (2005).

[17] R. J. Charity, L. G. Sobotka, and W. H. Dickhoff, Phys. Rev. Lett. **97**, 162503 (2006).

[18] C. Barbieri and W. H. Dickhoff, Int. J. Mod. Phys. A **24**, 2060 (2009).

[19] F. D. Becchetti Jr. and G. W. Greenlees, Phys. Rev. **182**, 1190 (1969).

[20] R. L. Varner, W. J. Thompson, T. L. McAbee, E. J. Ludwig, and T. B. Clegg, Phys. Rep. **201**, 57 (1991).

[21] A. J. Koning and J. P. Delaroche, Nucl. Phys. A **713**, 231 (2003).

[22] A. M. Lane, Nucl. Phys. **35**, 676 (1962).

[23] L. Hao, W. Sun, and E. S. Soukhovitskii, J. Phys. G: Nucl. Part. Phys. **35**, 095103 (2008).

[24] X. Li and C. Cai, Nucl. Phys. A **801**, 43 (2008).

[25] R. Shane, R. Charity, J. Elson, L. Sobotka, M. Devlin, N. Fotiades, and J. O'Donnell, Nucl. Instrum. Methods Phys. Res., Sect. A **614**, 468 (2010).

[26] S. M. El-Kadi, C. E. Nelson, F. O. Purser, R. L. Walter, A. Beyerle, C. R. Gould, and L. W. Seagondollar, Nucl. Phys. A **390**, 509 (1982).

[27] R. N. Pedroni, Ph.D. thesis, Duke University, 1986.

[28] R. A. Arndt, W. J. Briscoe, I. I. Strakovsky, and R. L. Workman, Phys. Rev. C **76**, 025209 (2007).

[29] W. Tornow *et al.*, Nucl. Phys. A **385**, 373 (1982).

[30] G. M. Honoré, W. Tornow, C. R. Howell, R. S. Pedroni, R. C. Byrd, R. L. Walter, and J. P. Delaroche, Phys. Rev. C **33**, 1129 (1986).

[31] S. Agostinelli *et al.*, Nucl. Instrum. Methods Phys. Res., Sect. A **506**, 250 (2003).

[32] M. Drosg and O. Schwerer, *Handbook on Nuclear Activation Data* (IAEA, Vienna, 1987).

[33] F. Perey and B. Buck, Nucl. Phys. **32**, 353 (1962).

[34] A. Nadasen, P. Schwandt, P. P. Singh, W. W. Jacobs, A. D. Bacher, P. T. Debevec, M. D. Kaitchuck, and J. T. Meek, Phys. Rev. C **23**, 1023 (1981).

[35] W. Tornow, Z. P. Chen, and J. P. Delaroche, Phys. Rev. C **42**, 693 (1990).

[36] J.-P. Jeukenne, A. Lejeune, and C. Mahaux, Phys. Rev. C **16**, 80 (1977).

[37] E. Bauge, J. P. Delaroche, and M. Girod, Phys. Rev. C **58**, 1118 (1998).

[38] J. P. Jeukenne and C. Mahaux, Nucl. Phys. A **394**, 445 (1983).

[39] W. T. H. van Oers, Phys. Rev. C **3**, 1550 (1971).

[40] T. Otsuka, T. Suzuki, R. Fujimoto, H. Grawe, and Y. Akaishi, Phys. Rev. Lett. **95**, 232502 (2005).

[41] G. W. Greenlees, G. J. Pyle, and Y. C. Tang, Phys. Rev. **171**, 1115 (1968).

[42] S. D. Wassenaar, P. J. van Hall, S. S. Klein, G. J. Nijgh, J. H. Polane, and O. J. Poppema, J. Phys. G: Nucl. Part. Phys. **15**, 181 (1989).

[43] R. H. McCamis *et al.*, Phys. Rev. C **33**, 1624 (1986).

[44] R. F. Carlson, A. J. Cox, T. Eliyakut-Roshko, and W. T. H. van Oers, Can. J. Phys. **73**, 512 (1995).

[45] R. F. Carlson, A. J. Cox, N. E. Davison, T. Eliyakut-Roshko, R. H. McCamis, and W. T. H. van Oers, Phys. Rev. C **49**, 3090 (1994).

[46] C. Mahaux and R. Sartor, Nucl. Phys. A **484**, 205 (1988).

[47] J.-P. Jeukenne, C. Mahaux, and R. Sartor, Phys. Rev. C **43**, 2211 (1991).

[48] J. M. Eisenberg and W. Greiner, *Nuclear Theory*, Vol.I (North-Holland, Amsterdam, 1987).

[49] P. A. Seeger, Los Alamos Science Laboratory Report No. LA-DC-8950a, 1968 (unpublished).

[50] W. D. Myers, *Droplet Model of Atomic Nuclei* (Plenum, New York, 1977).

[51] P. Danielewicz and J. Lee, Nucl. Phys. A **818**, 36 (2009); (private communication).

[52] J. P. Jeukenne, A. Lejeune, and C. Mahaux, Phys. Rep. **25**, 83 (1976).

[53] R. J. Rook, Nucl. Phys. A **222**, 596 (1974).

[54] M. F. van Batenburg, Ph.D. thesis, University of Utrecht, Netherlands, 2001.

[55] G. Audi, A. H. Wapstra, and C. Thibault, Nucl. Phys. A **729**, 337 (2003).

[56] G. J. Kramer *et al.*, Phys. Lett. B **227**, 199 (1989).

[57] G. J. Kramer, H. P. Blok, and L. Lapikás, Nucl. Phys. A **679**, 267 (2001).

[58] H. de Vries, C. W. de Jager, and C. de Vries, At. Data Nucl. Data Tables **36**, 495 (1987).

[59] M. Waroquier, J. Sau, K. Heyde, P. Van Isacker, and H. Vincx, Phys. Rev. C **19**, 1983 (1979).

[60] P. Fallon *et al.*, Phys. Rev. C **81**, 041302(R) (2010).

[61] Ø. Jensen, G. Hagen, M. Hjorth-Jensen, B. A. Brown, and A. Gade, arXiv:1104.1552v1.

[62] J. R. Erskine, A. Marinov, and J. P. Schiffer, Phys. Rev. **142**, 633 (1966).

[63] A. N. James, P. T. Andrews, P. Kirkby, and B. G. Lowe, Nucl. Phys. A **138**, 145 (1969).

[64] D. H. Youngblood, R. L. Kozub, R. A. Kenefick, and J. C. Hiebert, Phys. Rev. C **2**, 477 (1970).

[65] D. J. Millener and P. E. Hodgson, Nucl. Phys. A **209**, 59 (1973).

[66] P. Doll, G. J. Wagner, K. T. Knöpfle, and G. Mairle, Nucl. Phys. A **263**, 210 (1976).

[67] M. Matoba, O. Iwamoto, Y. Uozumi, T. Sakae, N. Koori, T. Fujiki, H. Ohgaki, H. Ijiri, T. Maki, and M. Nakano, Phys. Rev. C **48**, 95 (1993).

[68] Y. Uozumi, N. Kikuzawa, T. Sakae, M. Matoba, K. Kinoshita, T. Sajima, H. Ijiri, N. Koori, M. Nakano, and T. Maki, Phys. Rev. C **50**, 263 (1994).

[69] J. F. Dicello, G. Igo, W. T. Leland, and F. G. Perey, Phys. Rev. C **4**, 1130 (1971).

[70] E. T. Boschitz, R. W. Bercaw, and J. S. Vincent, Phys. Rev. Lett. **13**, 322 (1964).

[71] D. L. Watson, J. Lowe, J. C. Dore, R. M. Craig, and D. J. Baugh, Nucl. Phys. A **92**, 193 (1967).

[72] V. Hnizdo, O. Karban, J. Lowe, G. W. Greenlees, and W. Makofske, Phys. Rev. C **3**, 1560 (1971).

[73] L. N. Blumberg, E. E. G. Gross, A. van der Woude, A. Zucker, and R. H. Bassel, Phys. Rev. **147**, 812 (1966).

[74] R. M. Craig, J. C. Dore, J. Lowe, and D. L. Watson, Nucl. Phys. **86**, 113 (1966).

[75] C. B. Fulmer, J. B. Ball, A. Scott, and M. L. Whiten, Phys. Rev. **181**, 1565 (1969).

[76] T. Noro, H. Sakaguchi, M. Nakamura, K. Hatanaka, F. Ohtani, H. Sakamoto, and S. Kobayashi, Nucl. Phys. A **366**, 189 (1981).

[77] P. Schwandt, H. O. Meyer, W. W. Jacobs, A. D. Bacher, S. E. Vigdor, M. D. Kaitchuck, and T. R. Donoghue, Phys. Rev. C **26**, 55 (1982).

[78] H. Seifert, Ph.D. thesis, University of Maryland, 1990.

[79] C. Rolland, B. Geoffrion, N. Marty, M. Morlet, B. Tatischeff, and A. Willis, Nucl. Phys. **80**, 625 (1966).

[80] D. P. Murdock and C. J. Horowitz, Phys. Rev. C **35**, 1442 (1987).

[81] A. Marinov, L. L. Lee, and J. P. Schiffer, Phys. Rev. **145**, 852 (1966).

[82] J. C. Lombardi, R. N. Boyd, R. Arking, and A. B. Robbins, Nucl. Phys. A **188**, 103 (1972).

[83] H. S. Liers, Nucl. Phys. A **170**, 616 (1971).

[84] J. Rapaport, J. D. Carlson, D. Bainum, T. S. Cheema, and R. W. Finlay, Nucl. Phys. A **286**, 232 (1977).

[85] R. Alarcon, J. Rapaport, and R. W. Finlay, Nucl. Phys. A **462**, 413 (1987).

[86] R. P. DeVito, S. M. Austin, W. Sterrenburg, and U. E. P. Berg, Phys. Rev. Lett. **47**, 628 (1981).

[87] J. H. Osborne *et al.*, Phys. Rev. C **70**, 054613 (2004).

[88] S. F. Hicks, S. E. Hicks, G. R. Shen, and M. T. McEllistrem, Phys. Rev. C **41**, 2560 (1990).

[89] A. E. Antropov, P. P. Zarubin, P. D. Ioannu, B. N. Orlov, and V. S. Romanov, Bull. Acad. Sci. USSR, Phys. Ser. **40**(4), 102 (1976) [Izv. Akad. Nauk. SSSR, Ser. Fiz. **40**, 812 (1976)].

[90] M. Tomizawa, T. Aoki, Y. Aoki, T. Murayama, T. Sakai, Y. Tagishi, and K. Yagi, Phys. Rev. C **41**, 1486 (1990).

[91] J. C. Lombardi, R. N. Boyd, R. Arking, and A. B. Robbins, Nucl. Phys. A **192**, 641 (1972).

[92] R. L. Varner, Ph.D. thesis, Duke University, 1986.

[93] P. Kossanyi-Demay, R. de Swiniarski, and C. Glashausser, Nucl. Phys. A **94**, 513 (1967).

[94] A. Garin, C. Glashausser, A. Papineau, R. de Swiniarski, and J. Thirion, Phys. Lett. **21**, 73 (1966).

[95] B. M. Preedom, C. R. Gruhn, T. Y. T. Kuo, and C. J. Maggiore, Phys. Rev. C **2**, 166 (1970).

[96] H. Sakaguchi, M. Nakamura, K. Hatanaka, A. Goto, T. Noro, F. Ohtani, H. Sakamoto, H. Ogawa, and S. Kobayashi, Phys. Rev. C **26**, 944 (1982).

[97] L. Rosen and L. Stewart, Phys. Rev. Lett. **10**, 246 (1963).

[98] R. J. Peterson, Ann. Phys. (NY) **53**, 40 (1969).

[99] G. W. Greenlees, C. H. Poppe, J. A. Sievers, and D. L. Watson, Phys. Rev. C **3**, 1231 (1971).

[100] L. L. Lee and J. P. Schiffer, Phys. Rev. **134**, B765 (1964).

[101] P. J. V. Hall, J. P. M. G. Melssen, S. D. Wassenaar, O. J. Poppema, S. S. Klein, and G. J. Nijgh, Nucl. Phys. A **291**, 63 (1977).

[102] J. R. Tesmer and F. H. Schmidt, Phys. Rev. C **5**, 864 (1972).

[103] D. J. Baugh, M. J. Kenny, J. Lowe, D. L. Watson, and H. Wojciechowski, Nucl. Phys. A **99**, 203 (1967).

[104] E. Fabrici, S. Micheletti, M. Pignanelli, F. G. Resmini, R. De Leo, G. D'Erasmo, A. Pantaleo, J. L. Escudié, and A. Tarrats, Phys. Rev. C **21**, 830 (1980).

[105] E. Fabrici, S. Micheletti, M. Pignanelli, F. G. Resmini, R. De Leo, G. D'Erasmo, and A. Pantaleo, Phys. Rev. C **21**, 844 (1980).

[106] M. K. Brussel and J. H. Williams, Phys. Rev. **114**, 525 (1959).

[107] W. E. Kinney and F. G. Perey, Oak Ridge National Laboratory Report No. 4907, 1974 (unpublished).

[108] S. Mellema, R. W. Finlay, F. S. Dietrich, and F. Petrovich, Phys. Rev. C **28**, 2267 (1983).

[109] C. E. Floyd, P. P. Guss, R. C. Byrd, K. Murphy, R. L. Walter, and J. P. Delaroche, Phys. Rev. C **28**, 1498 (1983).

[110] R. S. Pedroni, C. R. Howell, G. M. Honoré, H. G. Pfutzner, R. C. Byrd, R. L. Walter, and J. P. Delaroche, Phys. Rev. C **38**, 2052 (1988).

[111] A. I. Tutubalin *et al.*, in *Proceeding of second National Soviet Conference on Neutron Physics, Kiev, 1973*, edited by L. N. Usachev, Vol. 3 (F.E.I. Obninsk, 1974), p. 62.

[112] N. Baron, R. F. Leonard, and D. A. Lind, Phys. Rev. **180**, 978 (1969).

[113] C. B. Fulmer, Phys. Rev. **125**, 631 (1962).

[114] R. M. Craig, J. C. Dore, G. W. Greenlees, J. S. Lilley, J. Lowe, and P. C. Rowe, Nucl. Phys. **58**, 515 (1964).

[115] B. W. Ridley and J. F. Turner, Nucl. Phys. **58**, 497 (1964).

[116] M. P. Fricke, E. E. Gross, and A. Zucker, Phys. Rev. **163**, 1153 (1967).

[117] D. C. Kocher, F. E. Bertrand, E. E. Gross, and E. Newman, Phys. Rev. C **14**, 1392 (1976).

[118] K. Kwiatkowski and N. S. Wall, Nucl. Phys. A **301**, 349 (1978).

[119] P. G. Roos and N. S. Wall, Phys. Rev. **140**, B1237 (1965).

[120] F. Hofmann *et al.*, Phys. Lett. B **612**, 165 (2005).

[121] A. Ingemarsson, T. Johansson, and G. Tibell, Nucl. Phys. A **365**, 426 (1981).

[122] H. Sakaguchi *et al.*, Phys. Rev. C **57**, 1749 (1998).

[123] C. M. Perey, F. G. Perey, J. K. Dickens, and R. J. Silva, Phys. Rev. **175**, 1460 (1968).

[124] S. Kobayashi, K. Matsuda, Y. Nagahara, Y. Oda, and N. Yamamuro, J. Phys. Soc. Jpn. **15**, 1151 (1960).

[125] D. J. Baugh, G. W. Greenlees, J. S. Lilley, and S. Roman, Nucl. Phys. **65**, 33 (1965).

[126] M. Koike, K. Matsuda, I. Nonaka, Y. Saji, K. Yagi, H. Ejiri, Y. Ishizaki, Y. Nakajima, and E. Tanaka, J. Phys. Soc. Jpn. **21**, 2103 (1966).

[127] P. J. Dallimore, W. F. Davidson, and J. Hellström, Nucl. Phys. A **132**, 287 (1969).

[128] W. Makofske, G. W. Greenlees, H. S. Liers, and G. J. Pyle, Phys. Rev. C **5**, 780 (1972).

[129] H. S. Liers, R. N. Boyd, C. H. Poppe, J. A. Sievers, and D. L. Watson, Phys. Rev. C **2**, 1399 (1970).

[130] V. Comparat, R. Frascaria, N. Marty, M. Morlet, and A. Willis, Nucl. Phys. A **221**, 403 (1974).

[131] A. B. Smith, P. T. Guenther, J. F. Whalen, and S. Chiba, J. Phys. G: Nucl. Part. Phys. **18**, 629 (1992).

[132] P. P. Guss, R. C. Byrd, C. E. Floyd, C. R. Howell, K. Murphy, G. Tungate, R. S. Pedroni, R. L. Walter, J. P. Delaroche, and T. B. Clegg, Nucl. Phys. A **438**, 187 (1985).

[133] Y. Yamanouti, J. Rapaport, S. M. Grimes, V. Kulkarni, R. W. Finlay, D. Bainum, P. Grabmayr, and G. Randers-Pehrson, Brookhaven National Laboratory Report No. 51245, 1980 (unpublished).

[134] I. A. Korzh, V. P. Lunev, V. A. Mishchenko, E. N. Mozhzhukhin, M. V. Pasechnik, and N. M. Pravdivyy, Yad. Fiz. **31**, 13 (1980) [Sov. J. Nucl. Phys. **31**, 5 (1980)].

[135] A. F. Gurbich and N. N. Titarenko, Vopr. At. Nauki. Tekh., Ser. Yad. Konst. **2**, 142 (1996).

[136] J. K. Dickens, E. Eichler, and G. R. Satchler, Phys. Rev. **168**, 1355 (1968).

[137] K. Matsuda, H. Nakamura, I. Nonaka, H. Taketani, T. Wada, Y. Awaya, and M. Koike, J. Phys. Soc. Jpn. **22**, 1311 (1967).

[138] W. S. Gray, R. A. Kenefick, J. J. Kraushaar, and G. R. Satchler, Phys. Rev. **142**, 735 (1966).

[139] C. Glashausser, R. de Swiniarski, J. Goudergues, R. M. Lombard, B. Mayer, and J. Thirion, Phys. Rev. **184**, 1217 (1969).

[140] J. B. Ball, C. B. Fulmer, and R. H. Bassel, Phys. Rev. **135**, B706 (1964).

[141] L. T. V. D. Bijl, H. P. Blok, J. F. A. V. Hienen, and J. Blok, Nucl. Phys. A **393**, 173 (1983).

[142] R. de Swiniarski, Dinh-Lien Pham, and G. Bagieu, Can. J. Phys. **55**, 43 (1977).

[143] M. P. Fricke, E. E. Gross, B. J. Morton, and A. Zucker, Phys. Rev. **156**, 1207 (1967).

[144] G. S. Mani, D. T. Jones, and D. Jacques, Nucl. Phys. A **165**, 384 (1971).

[145] E. Hagberg, A. Ingemarsson, and B. Sundqvist, Phys. Scr. **3**, 245 (1971).

[146] S. J. Burger and G. Heymann, Nucl. Phys. A **243**, 461 (1975).

[147] H. F. Lutz, D. W. Heikkinen, and W. Bartolini, Phys. Rev. C **4**, 934 (1971).

[148] B. C. Sinha, V. R. W. Edwards, E. J. Burge, and W. H. Tait, Nucl. Phys. A **183**, 401 (1972).

[149] E. Cereda, M. Pignanelli, S. Micheletti, H. V. von Geramb, M. N. Harakeh, R. De Leo, G. D'Erasmo, and A. Pantaleo, Phys. Rev. C **26**, 1941 (1982).

[150] J. Rapaport, T. S. Cheema, D. E. Bainum, R. W. Finlay, and J. D. Carlson, Nucl. Phys. A **313**, 1 (1979).

[151] W. Makofske, W. Savin, H. Ogata, and T. H. Kruse, Phys. Rev. **174**, 1429 (1968).

[152] A. Hardacre, J. Turner, J. Kerr, G. Gard, P. Cavanagh, and C. Coleman, Nucl. Phys. A **173**, 436 (1971).

[153] D. J. Abbott, T. B. Clegg, and J. P. Delaroche, Phys. Rev. C **35**, 2028 (1987).

[154] R. N. Boyd and G. W. Greenlees, Phys. Rev. **176**, 1394 (1968).

[155] L. W. Put, P. P. Urone, and A. M. J. Paans, Phys. Lett. B **35**, 311 (1971).

[156] R. M. Craig, J. C. Dore, G. W. Greenlees, J. S. Lilley, and J. Lowe, Nucl. Phys. **58**, 515 (1964).

[157] S. Kailas, P. P. Singh, D. L. Friesel, C. C. Foster, P. Schwandt, and J. Wiggins, Phys. Rev. C **29**, 2075 (1984).

[158] J. Rapaport, M. Mirzaa, H. Hadizadeh, D. E. Bainum, and R. W. Finlay, Nucl. Phys. A **341**, 56 (1980).

[159] W. Kretschmer, H. Löh, K. Spitzer, and W. Stach, Phys. Lett. B **87**, 343 (1979).

[160] J. S. Eck and W. J. Thompson, Nucl. Phys. A **237**, 83 (1975).

[161] R. Rathmell and W. Haeberli, Nucl. Phys. A **178**, 458 (1972).

[162] W. T. H. van Oers, H. Haw, N. E. Davison, A. Ingemarsson, B. Fagerström, and G. Tibell, Phys. Rev. C **10**, 307 (1974).

[163] G. W. Greenless, V. Hnizdo, O. Karban, J. Lowe, and W. Makofske, Phys. Rev. C **2**, 1063 (1970).

[164] A. Willis, B. Geoffrion, N. Marty, M. Morlet, C. Rolland, and B. Tatischeff, Nucl. Phys. A **112**, 417 (1968).

[165] L. Lee *et al.*, Phys. Lett. B **205**, 219 (1988).

[166] J. R. M. Annand, R. W. Finlay, and P. S. Dietrich, Nucl. Phys. A **443**, 249 (1985).

[167] M. L. Roberts, P. D. Felsher, G. J. Weisel, Z. Chen, C. R. Howell, W. Tornow, R. L. Walter, and D. J. Horen, Phys. Rev. C **44**, 2006 (1991).

[168] J. Rapaport, T. S. Cheema, D. E. Bainum, R. W. Finlay, and J. D. Carlson, Nucl. Phys. A **296**, 95 (1978).

[169] J. P. Delaroche, C. E. Floyd, P. P. Guss, R. C. Byrd, K. Murphy, G. Tungate, and R. L. Walter, Phys. Rev. C **28**, 1410 (1983).

[170] C. E. Floyd, P. P. Guss, K. Murphy, C. R. Howell, R. C. Byrd, G. Tungate, S. A. Wender, R. L. Walter, and T. B. Clegg, Phys. Rev. C **25**, 1682 (1982).

[171] L. F. Hansen, F. S. Dietrich, B. A. Pohl, C. H. Poppe, and C. Wong, Phys. Rev. C **31**, 111 (1985).

[172] C. E. F. Jr., Ph.D. thesis, Triangle Uinversities Nuclear Laboratory, 1981.

[173] R. W. Finlay, J. R. M. Annand, T. S. Cheema, J. Rapaport, and F. S. Dietrich, Phys. Rev. C **30**, 796 (1984).

[174] R. P. Devito, Ph.D. thesis, Michigan State University, 1980.

[175] A. Öhrn *et al.*, Phys. Rev. C **77**, 024605 (2008).

[176] J. F. Dicello and G. Igo, Phys. Rev. C **2**, 488 (1970).

[177] R. F. Carlson, A. J. Cox, J. R. Nimmo, N. E. Davison, S. A. Elbakr, J. L. Horton, A. Houdayer, A. M. Sourkes, W. T. H. van Oers, and D. J. Margaziotis, Phys. Rev. C **12**, 1167 (1975).

[178] J. F. Turner, B. W. Ridley, P. E. Cavanagh, G. A. Gard, and A. H. Hardacre, Nucl. Phys. **58**, 509 (1964).

[179] Y. V. Dukarevich, A. N. Dyumin, and D. M. Kaminker, Nucl. Phys. A **92**, 433 (1967).

[180] P. Boschung, J. T. Lindow, and E. F. Shrader, Nucl. Phys. A **161**, 593 (1971).

[181] P. Stoler, J. Clement, C. Goulding, and R. Fairchild, in *Proceeding of the Third Conference on Neutron Cross Sections and Techniques, Knoxville, Tennessee, 1971*, edited by R. L. Macklin, CONF-710301, Vol. 1 (US AEC Division of Technical Information, Oak Ridge, Tenn., 1971) , p. 311.

[182] A. Smith, P. Guenther, D. Smith, and J. Walen, Nucl. Sci. Eng. **72**, 293 (1979).

[183] C. I. Zanelli, P. P. Urone, J. L. Romero, F. P. Brady, M. L. Johnson, G. A. Needham, J. L. Ullmann, and D. L. Johnson, Phys. Rev. C **23**, 1015 (1981).

[184] D. G. Foster Jr. and D. W. Glasgow, Phys. Rev. C **3**, 576 (1971).

[185] D. C. Larson, J. Harvey, and N. M. Hill, Brookhaven National Laboratory Report No. BNL-BNS-51245, 1980 (unpublished).

[186] C. I. Zanelli, F. P. Brady, J. L. Romero, C. M. Castaneda, and D. L. Johnson, Phys. Rev. C **33**, 66 (1986).

[187] W. P. Abfalterer, F. B. Bateman, F. S. Dietrich, R. W. Finlay, R. C. Haight, and G. L. Morgan, Phys. Rev. C **63**, 044608 (2001).

[188] J. F. Dicello, G. J. Igo, and M. L. Roush, Phys. Rev. **157**, 1001 (1967).

[189] J. J. H. Menet, E. E. Gross, J. J. Malanify, and A. Zucker, Phys. Rev. C **4**, 1114 (1971).

[190] J. J. H. Menet, E. E. Gross, J. J. Malanify, and A. Zucker, Phys. Rev. Lett. **22**, 1128 (1969).

[191] A. Auce *et al.*, Phys. Rev. C **71**, 064606 (2005).

[192] H. S. Camarda, T. W. Phillips, and R. M. White, Phys. Rev. C **34**, 810 (1986).

[193] A. Ingemarsson *et al.*, Nucl. Phys. A **653**, 341 (1999).

[194] K. Bearpark, W. R. Graham, and G. Jones, Nucl. Phys. **73**, 206 (1965).

[195] T. Eliyakut-Roshko, R. H. McCamis, W. T. H. van Oers, R. F. Carlson, and A. J. Cox, Phys. Rev. C **51**, 1295 (1995).

[196] G. M. Haas and P. L. Okhuysen, Phys. Rev. **132**, 1211 (1963).

[197] R. W. Finlay, W. P. Abfalterer, G. Fink, E. Montei, T. Adami, P. W. Lisowski, G. L. Morgan, and R. C. Haight, Phys. Rev. C **47**, 237 (1993).

[198] J. W. A. den Herder, H. P. Blok, E. Jans, P. H. M. Keizer, L. Lapikás, E. N. M. Quint, G. van der Steenhoven, and P. K. A. de Witt Huberts, Nucl. Phys. A **490**, 507 (1988).

[199] E. N. M. Quint, Ph.D. thesis, University of Amsterdam, 1988.

[200] G. van der Steenhoven (private communication).